The Role of Vertical Wind Shear in Modulating Maximum Supercell Updraft Velocities

JOHN M. PETERS

Department of Meteorology, Naval Postgraduate School, Monterey, California

CHRISTOPHER J. NOWOTARSKI

Department of Atmospheric Sciences, Texas A&M University, College Station, Texas

HUGH MORRISON

National Center for Atmospheric Research, Boulder, Colorado

(Manuscript received 15 April 2019, in final form 10 June 2019)

ABSTRACT

Observed supercell updrafts consistently produce the fastest mid- to upper-tropospheric vertical velocities among all modes of convection. Two hypotheses for this feature are investigated. In the dynamic hypothesis, upward, largely rotationally driven pressure gradient accelerations enhance supercell updrafts relative to other forms of convection. In the thermodynamic hypothesis, supercell updrafts have more low-level inflow than ordinary updrafts because of the large vertical wind shear in supercell environments. This large inflow makes supercell updrafts wider than that of ordinary convection and less susceptible to the deleterious effects of entrainment-driven updraft core dilution on buoyancy. These hypotheses are tested using a large suite of idealized supercell simulations, wherein vertical shear, CAPE, and moisture are systematically varied. Consistent with the thermodynamic hypothesis, storms with the largest storm-relative flow have larger inflow, are wider, have larger buoyancy, and have faster updrafts. Analyses of the vertical momentum forcing along trajectories shows that maximum vertical velocities are often enhanced by dynamic pressure accelerations, but this enhancement is accompanied by larger downward buoyant pressure accelerations than in ordinary convection. Integrated buoyancy along parcel paths is therefore a strong constraint on maximum updraft speeds. Thus, through a combination of processes consistent with the dynamic and thermodynamic hypotheses, supercell updrafts are able to realize a larger percentage of CAPE than ordinary updrafts.

1. Introduction

Vertical velocities in supercell updrafts feature the most intense observed updraft speeds among all modes of atmospheric convection (Lehmiller et al. 2001). For instance, the 29 May 2012 Kingfisher, Oklahoma, supercell featured a dual-Doppler-estimated 65 $\mathrm{m\,s^{-1}}$ updraft in the middle troposphere (DiGangi et al. 2016), which substantially exceeds all the vertical velocity observations in nonsupercellular convection in the literature that we are aware of. The large vertical velocities in supercells facilitate production of the largest observed hailstones on Earth (e.g., Wakimoto et al. 2004), produce higher cross-tropopause mass transport than ordinary convection (Mullendore et al. 2005) and result in a higher mass detrainment level (Mullendore et al. 2013). Furthermore, supercell updrafts are capable of producing intense low-level vertical accelerations and associated stretching of vertical vorticity, which facilitates tornadogenesis (Markowski and Richardson 2014). The impressive organizational structure and intensity of supercells has long been attributed to the presence of strong vertical wind shear in these storms' environments, yet there remain aspects of the relationship between shear and updraft intensity that require further clarification. In particular, it is unclear from previous literature what role shear plays in modulating maximum updraft velocities in the middle and upper troposphere.

One potential explanation for why supercell updrafts are so intense is that upward buoyant accelerations in the mid- to upper-level updraft become increasingly

Corresponding author: J. Peters, jmpeters@nps.edu

DOI: 10.1175/JAS-D-19-0096.1

enhanced by upward dynamic accelerations associated with the supercell updraft's rotationally driven low pressure as environmental shear increases (hereafter the ''dynamic hypothesis''). Previous studies have shown evidence that maximum vertical velocities in nonsupercellular convection are primarily determined by buoyancy and buoyancy pressure forcing (e.g., Peters 2016; Morrison and Peters 2018), so it is possible that the addition of rotationally driven dynamic pressure accelerations in supercells is responsible for the stronger observed maximum updraft speeds than in nonsupercellular updrafts. Indeed, at *lower altitudes* supercell updrafts are substantially enhanced by the upward pressure gradient force caused by dynamically lowered pressure associated with the mesocyclone's vorticity maximum (Coffer and Parker 2015), which in turn plays a critical role in tornadogenesis (Markowski and Richardson 2014; Coffer et al. 2017). Furthermore, analyses of momentum budgets along trajectories in simulations have shown accelerations by dynamic pressure forcing that are comparable in magnitude to accelerations from buoyancy forces through a substantial portion of a supercell's updraft depth (e.g., Weisman and Klemp 1984, their Fig. 13; McCaul and Weisman 1996, their Fig. 12; Weisman and Rotunno 2000, their Fig. 13). The results of those studies imply that dynamic accelerations enhance maximum updraft speeds by 50%–100% over the values they would attain if buoyancy were acting alone. This lends credence to the dynamic hypothesis; however, those authors specifically focused on trajectories that passed through the maximum vertical velocity at 3-km height, and it is unclear whether this momentum budget analysis is representative of parcels that reach the overall updraft maximum in the upper troposphere. The spatial resolution of those simulations was relatively coarse by today's standards, with horizontal and vertical grid spacing of 1 km and 250 m, respectively. Furthermore, the simulations contained no ice microphysics, which could potentially lead to an underrepresentation of mid- to upper-level buoyancy. Given the recently demonstrated substantial sensitivities of the structure of simulated deep convection to model resolution (Bryan and Fritsch 2002; Bryan and Morrison 2012; Varble et al. 2014; Lebo and Morrison 2015; Potvin and Flora 2015) and the inclusion of ice physics (McCaul and Cohen 2002), a reexamination of vertical momentum budgets in supercell updrafts with state-of-the-art, high-resolution (e.g., few-hundred-meter grid spacing) numerical models is warranted.

An alternative hypothesis for the large vertical velocities in supercell updrafts is that supercell updrafts are more resistant to entrainment-driven dilution than nonsupercellular convection, and that they have larger buoyancy, buoyant accelerations, and vertical velocities as a consequence (hereafter the ''thermodynamic hypothesis''). This hypothesis is inspired by recent studies that have found that the updraft speed, rainfall production, and mesocyclone width of supercell thunderstorms scale proportionally with the deep-layer shear magnitude (e.g., Warren et al. 2017; Trapp et al. 2017). It was argued by Warren et al. (2017) that stronger shear equates to stronger low-level storm-relative flow, and that the stronger associated updraft inflow was responsible for the positive correlation between shear and updraft width. A reason for the intensity advantage of wide updrafts may be related to the entrainment of dry midtropospheric air; the cores of narrower updrafts are more susceptible to entrainment-driven reductions in buoyancy when compared to wider updrafts (e.g., Holton 1973; Kuo and Raymond 1980; Romps and Kuang 2010; Morrison 2017; Hannah 2017; Hernandez-Deckers and Sherwood 2018). It is therefore reasonable to hypothesize that storms within strongly sheared environments, like supercells, may have stronger updrafts than storms within weakly sheared environments because, in a given thermodynamic environment, cores of supercells are wider and therefore more buoyant. It should be noted that the thermodynamic and dynamic hypotheses are not exclusive of one another, and it is conceivable that both these processes play a role in determining supercell updraft intensities.

The purpose of this study is to evaluate the viability and relative importance of each of these hypotheses. A large suite of idealized supercell simulations (described in section 2) were initialized with horizontally homogeneous base-state environments combining various amounts of low-level shear, deep-layer shear, convective available potential energy (CAPE), and midlevel relative humidity. The results of these simulations are analyzed in section 3. Theoretical arguments explaining the physical basis for the simulation results are presented in section 4. Finally, section 5 provides a discussion and the conclusions.

2. Experiment design

a. Numerical modeling setup

All simulations were run with Cloud Model 1 (CM1; Bryan and Fritsch 2002), version 18. CM1 is a nonhydrostatic compressible model designed to simulate cloud processes in environments with idealized initial conditions (ICs) and lateral boundary conditions (LBCs). Bottom and top boundary conditions were free slip, and the simulations did not contain radiation physics

TABLE 1. Summary of the CM1 configuration.

Attribute	Value/setting	Notes
Fully compressible	Yes	
Horizontal grid spacing	250 m	
Vertical grid spacing	100 m	
Vertical coordinate	Height (m)	
Number of x and y points	400 × 400	
Vertical points	180	
Top and bottom LBCs	Free slip	
North and south LBCs	Open radiative	Durran and Klemp (1983)
East and west LBCs	Open radiative	Durran and Klemp (1983)
Convection initiation	Warm bubble at domain center; horizontal radius: 5 km; vertical radius: 1.4 km; θ perturbation: 3 K	
Microphysics	Morrison	Morrison et al. (2009)
Diffusion	Sixth order	
Subgrid turbulence	TKE	
Rayleigh dampening	Yes	
Dissipative heating	Yes	
Second- and sixth-order diffusion coefficient	75–0.04	
Longwave radiation	None	
Shortwave radiation	None	
Surface layer	None	
Boundary layer physics	None	
Cumulus parameterization	None	

or surface–atmosphere exchange. Microphysical processes were represented by the Morrison et al. (2009) double-moment scheme. LBCs were "open radiative" using the method of Durran and Klemp (1983). The horizontal grid spacing Δx was set to 250 m, the grid dimensions were 100 km in the x and y directions, and data were output every 5 min. The domain top was set to 18 km with a vertical grid spacing of 100 m. Various domain sizes (e.g., 200 km × 200 km) and grid spacings (e.g., 500 m and 1 km) were tested, and the results presented herein were insensitive to the domain size and grid spacing. We also tested the sensitivity of our results to variations in the initial bubble size and in the depth of the model domain, with no effect on our overall conclusions. The model was initialized with a passive tracer having a concentration of 100% below 1 km and 0% elsewhere to quantify the dilution of updraft cores via entrainment. Finally, Coriolis acceleration of all wind components was neglected. The model configuration is summarized in Table 1.

The initial soundings used in the CM1 simulations were based on the analytic thermodynamic sounding of Weisman and Klemp (1982, hereafter WK82; the WK82 sounding) and the analytic "quarter circle" wind profile of (Rotunno and Klemp 1982). To compare the influences of shear on updraft intensity to the influences of other environmental factors that may regulate updraft intensity, and to assure that the results presented later apply over a broad range of convective environments, simulations were run using 54 separate combinations of initial thermodynamic and wind profiles that were produced by systematic modifications to the WK82 sounding and quarter-circle wind profile (Figs. 1a,b). The relative humidity (RH) in the WK82 profile was modified to be constant above 3 km, and to decrease at a linear rate from the value in the original WK82 configuration at 1.7 km to the constant value at 3 km. This provided a simple method to test the sensitivity of simulated results to low (45%, denoted R45) and high (80%, denoted R80) mid- to upper-tropospheric RH. Boundary layer water vapor mixing ratios of 12 g kg^{-1} (0–1-km mean CAPE of 843 J kg^{-1}, denoted CAPE1), 14 g kg^{-1} (0–1-km mean CAPE of 1729 J kg^{-1}, denoted CAPE2), and 16 g kg^{-1} (0–1-km mean CAPE of 2744 J kg^{-1}, denoted CAPE3) were also used in the simulations to test the sensitivity of the results to low-level moisture and CAPE. The quarter-circle profile was modified from its original configuration so that all the directional shear was contained within the lowest 1 km (rather than 2 km in the original configuration), which is consistent with observed supercell and tornado environments (e.g., Markowski et al. 2003; Parker 2014). The magnitude of the 0–1-km shear in the v direction from the original quarter-circle profile was multiplied by 0.5 (denoted LL1), 1 (denoted LL2), and 1.5 (denoted LL3) to produce three different low-level shear profiles (Fig. 1b). Similarly, the magnitude of the 1–6-km shear

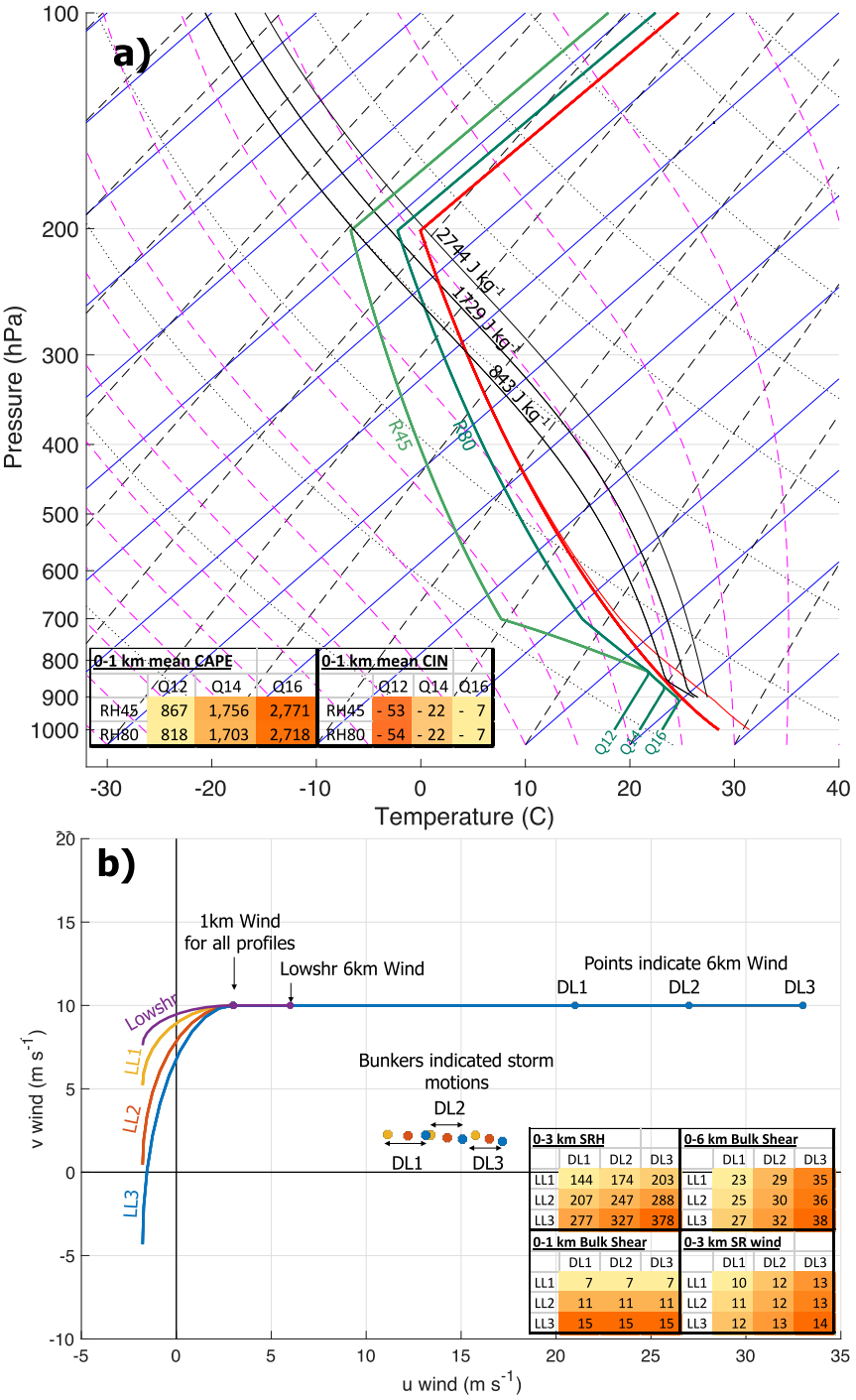

FIG. 1. (a) Skew T–log$p$ diagram of the thermodynamic profiles used to initialize CM1. Thick red line: temperature (°C); thin red line: virtual temperature (°C) for the RH80 and CAPE3 runs; black lines: temperature (°C) of lifted air parcel with the average properties of the lowest 1 km of the atmosphere from the CAPE1, CAPE2, and CAPE3 profiles; green lines: dewpoint temperature profiles from the CAPE1, CAPE2, and CAPE3 runs. The table in the lower-left corner shows the CAPE and CIN for each profile, with more red (more yellow) background colors of table entries indicating larger (smaller) magnitudes. (b) Hodograph of the wind profiles (m s^{-1}) used to initialize CM1. Yellow line: LL1; red line: LL2; blue line: LL3; purple line: LOWSHR. Storm-motion vectors estimated using the Bunkers et al. (2000) method are shown as solid dots (estimates for the LOWSHR profile are

in the original quarter circle profile was multiplied by 0.75 (denoted DL1), 1 (denoted DL2), and 1.25 (denoted DL3) to produce three different deep-layer shear profiles (Fig. 1b). An example of how simulations are named in the text is CAPE1_RH45_LL1_DL1, indicating that the base state used the thermodynamic characteristics CAPE1, RH45, and the wind characteristics LL1 and DL1. To center updrafts within the domain, domain translations speeds u_{move} and v_{move} were determined via the ad hoc formula $u_{\text{move}} = (3/4)u_{\text{Bunk}}$ and $v_{\text{move}} = v_{\text{Bunk}} - \psi + 2\,\text{m s}^{-1}$, where $\psi \equiv \max[\min(I_{\text{LL}}, I_{\text{CAPE}}) - 1, 0]$, I_{LL} and I_{CAPE} are the low-level shear and CAPE indices from our nomenclature for a given run (i.e., $I_{\text{LL}} = 1$ and $I_{\text{CAPE}} = 3$ for the CAPE3_RH45_LL1_DL1 run), and u_{Bunk} and v_{Bunk} are the right-moving storm-motion estimates from the Bunkers et al. (2000) method.

To compare the characteristics of supercellular convection to that of "ordinary convection," we performed three additional runs with the low-level shear magnitude of the quarter-circle profile multiplied by 0.25 and the deep-layer shear magnitude multiplied by 0.125 (Fig. 1b), and the CAPE1_RH85, CAPE2_RH85, and CAPE3_RH85 thermodynamic profiles. The 0–6-km shear in these runs was considerably weaker than that of the other runs, at roughly 7.5 m s^{-1}, and we will refer to these collectively as the LOWSHR runs.

b. *Defining, tracking, and assessing characteristics of supercell updrafts*

Most simulations produced initial left- and right-moving supercell pairs, as well as secondary supercells and sometimes large regions of nonsupercellular convection. The remainder of the analysis concentrates on the initial right-moving supercell, which was generally the dominant storm in terms of size and updraft intensity. Because of the large number of simulations analyzed, a method was devised to identify and track the dominant right-moving supercell objectively. First, the 0–4-km mean vertical velocity $\overline{w}|_{0-4\text{km}}$ and vertical vorticity $\overline{\zeta}|_{0-4\text{km}}$ were computed at each time step. Continuous regions where both $\overline{w}|_{0-4\text{km}} > 3\,\text{m s}^{-1}$ and $\overline{\zeta}|_{0-4\text{km}} > 0\,\text{s}^{-1}$ were then identified. The initial right-moving storm was assumed to correspond to the largest such region. The center point (x_s, y_s) of the supercell updraft was defined as the updraft helicity (UH $\equiv \overline{\zeta}|_{0-4\text{km}}\overline{w}|_{0-4\text{km}}$) weighted average of the locations of all points contained within the identified region. Continuous 2D slices of $w > 3\,\text{m s}^{-1}$ on each vertical level were first used to define the 3D extent of the updraft. We next found the index k of the highest vertical level z_k where $w > 3\,\text{m s}^{-1}$ at the updraft center point (so far, this level will have been the top of the updraft). The remainder of the updraft's vertical extent above z_k was defined by finding a continuous 3D region of $w > 3\,\text{m s}^{-1}$ above z_{k-1} that the contained the updraft center point at z_k. This last step accounted for the potential for an updraft to slant sufficiently far away from the center point in the upper troposphere so that it no longer contained the updraft center point at upper levels.

After this objective procedure, supercell center tracks in conjunction with simulated radar reflectivity factor snapshots were then subjectively assessed to remove erroneous storm locations. Storm-motion vectors $\mathbf{C}_x$ and $\mathbf{C}_y$ were computed by smoothing the storm position time series' x_s and y_s with a Gaussian filter with a radius of influence of 10 min to get X_s and Y_s, and computing $\mathbf{C}_x = dX_s/dt \approx [X_s(t + \Delta t) - X_s(t - \Delta t)]/2\Delta t$ and $\mathbf{C}_y = dY_s/dt \approx [Y_s(t + \Delta t) - Y_s(t - \Delta t)]/2\Delta t$, where $\Delta t = 5$ min is the time interval of the output data. Storm motions at the first and last points in the lifetime of tracked supercells were computed using linear interpolation from temporally adjacent points.

In subsequent analysis, most quantities were either horizontally averaged over the updraft region (denoted by "mean"), or were represented by the maximum of that quantity at a given level (denoted by "max"). These quantities were then vertically averaged over a given height range to give a single data point for each 5-min output time from a given run. The average horizontal inflow/outflow of air across the updraft boundary u_{inf} at a given height is

$$u_{\text{inf}} = \frac{1}{\sigma}\oint(\mathbf{V} - \mathbf{C}) \cdot \hat{\mathbf{n}}\, d\sigma = \frac{1}{\sigma}\iint_{\delta A} \nabla_H \cdot \mathbf{V}\, dA, \qquad (1)$$

where $\hat{\mathbf{n}}$ is a horizontal unit vector normal to the updraft edge, $\mathbf{V}$ is the ground-relative wind from the simulation, $\mathbf{C}$ is the storm-motion vector, and A and σ are the updraft area and perimeter length at a given height. The word "inflow" will be used to describe u_{inf}, which is the direct flow of air across an updraft's periphery. In contrast, "storm-relative (SR) flow" refers to the flow-field outside the updraft with the storm motion subtracted.

←

omitted since those runs did not produce supercells). The table in the lower-right corner shows the 0–3-km SR helicity (SRH), 0–6-km bulk shear, 0–1-km bulk shear, and 0–3-km mean storm-relative wind magnitudes.

Note that not all storm-relative flow is guaranteed to cross into an updraft as inflow. Finally, all updraft radii obtained from simulations are defined at a given height as $R_{\text{eff}} \equiv \sqrt{A/\pi}$.

c. Vertical accelerations

The anelastic inviscid vertical momentum equation was used to assess the influence of environmental characteristics on updraft accelerations and vertical velocities. This equation is written as

$$\frac{dw}{dt} = \underbrace{\underbrace{B - \frac{1}{\rho_0}\frac{\partial p_b}{\partial z}}_{\text{BPA}} - \underbrace{\frac{1}{\rho_0}\frac{\partial p_d}{\partial z}}_{\text{DPA}}}_{\text{EBPA}}, \tag{2}$$

where $B \equiv -g\rho'/\rho_0 - g\sum r_i$, r_i is the ith hydrometeor species mixing ratio, $\vartheta_0(z)$ is the initial model profile of an arbitrary variable ϑ, $\vartheta' \equiv \vartheta - \vartheta_0$, and the definitions of p_b and p_d are

$$\nabla^2 p_b = \frac{\partial \rho_0 B}{\partial z}, \quad \nabla^2 p_d = -\nabla \cdot [\rho_0(\mathbf{V} \cdot \nabla)\mathbf{V}]. \tag{3}$$

The second term on the rhs of Eq. (2) is known as buoyancy pressure acceleration (BPA), the third term is known as dynamic pressure acceleration (DPA), and the sum of B and BPA is often called effective buoyancy pressure acceleration (EBPA) (Davies-Jones 2003; Doswell and Markowski 2004; Jeevanjee and Romps 2016; Peters 2016). Because BPA is strictly a function of density and buoyancy, it is exclusively determined by an updraft's thermodynamic properties and typically, though not always, acts in opposition to the buoyancy force (e.g., Doswell and Markowski 2004; Morrison 2016a). DPA, on the other hand, is primarily associated with spatial gradients in wind velocity, and is often dominated at low to midlevels by upward accelerations beneath a supercell mesocyclone's rotationally driven dynamic pressure minimum (e.g., Weisman and Rotunno 2000), and at upper levels by both upward and downward accelerations associated with updrafts' ring-vortex-like toroidal circulations (Morrison and Peters 2018). Here the pressure contributions were obtained by computing the right-hand sides of Eqs. (3) from model output, discretizing the Laplacian as second-order centered finite differences, applying a two-dimensional discrete Fourier transform in the horizontal direction, solving the resultant tridiagonal matrix equation in Fourier space, and then inverting the two-dimensional Fourier transform (this is the method used in CM1 when the model is run in anelastic mode).

Equation (2) was integrated from time t_1 to t_2 to obtain the individual contributions to the change in an air parcel's vertical velocity by the different acceleration terms:

$$w_{\text{NET}}(t_2) \equiv w(t_2) - w(t_1) = \underbrace{\underbrace{\int_{t_1}^{t_2} B\,dt}_{w_B} - \underbrace{\int_{t_1}^{t_2} \frac{1}{\rho_0}\frac{\partial p_b}{\partial z}\,dt}_{w_{\text{BPA}}}}_{w_{\text{EBPA}}} - \underbrace{\int_{t_1}^{t_2} \frac{1}{\rho_0}\frac{\partial p_d}{\partial z}\,dt}_{w_{\text{DPA}}}. \tag{4}$$

Momentum budgets along trajectories were computed to evaluate the relative roles of buoyant and dynamic accelerations in determining maximum updraft velocities. To compute these trajectories, each run was restarted at the 120-min mark and run for 20 min with a 5-s model output frequency. Starting at minute 127 and ending at minute 132.25, back and forward trajectories were released every 15 s from the grid point with the domain maximum w, if a tracked updraft was present. Forward and backward integration was approximated with an Eulerian time discretization. Back trajectories were run for 6.5 min, forward trajectories were run for 1.25 min, and the back and forward trajectories were connected to make a 7.75-min continuous trajectory path. Because of the extremely fast updraft velocities present in some simulations (sometimes $>70\,\text{m s}^{-1}$), atmospheric data were linearly temporally interpolated onto $\lceil w_{\text{traj}}\Delta t/0.6\Delta z \rceil$ evenly spaced intervals between the 5-s model output times to increase the accuracy of trajectory position estimates, where $\Delta t = 5$ s, $\Delta z = 100$ m, and w_{traj} is the vertical velocity at a given time along the trajectory. Once a trajectory path was established, the individual terms on the right-hand side of Eq. (4) were estimated by interpolating quantities onto individual trajectory points. Henceforth, w_{traj} refers to the vertical velocity directly interpolated onto the trajectory path, whereas w_{NET} refers to the sum of the right-hand-side terms in Eq. (4). Trajectories were only considered "accurate" and used in further analysis if $100|[\max(w_{\text{traj}}) - \max(w_{\text{NET}})]/[\max(w_{\text{traj}}) - w_{\text{traj},0}]| < 10\%$ (where $w_{\text{traj},0}$ is the initial vertical velocity along the trajectory), indicating that the error in $\max(w)$ predicted by Eq. (4) is less than 10%. We further required that $\max(w_{\text{traj}})$ and $\max(w_{\text{NET}})$ occurred at the same point along a trajectory.

To quantify the effects on w from dynamic and total pressure forcing, we must estimate what w would have been if EBPA or buoyancy were acting alone. To accomplish this, we write

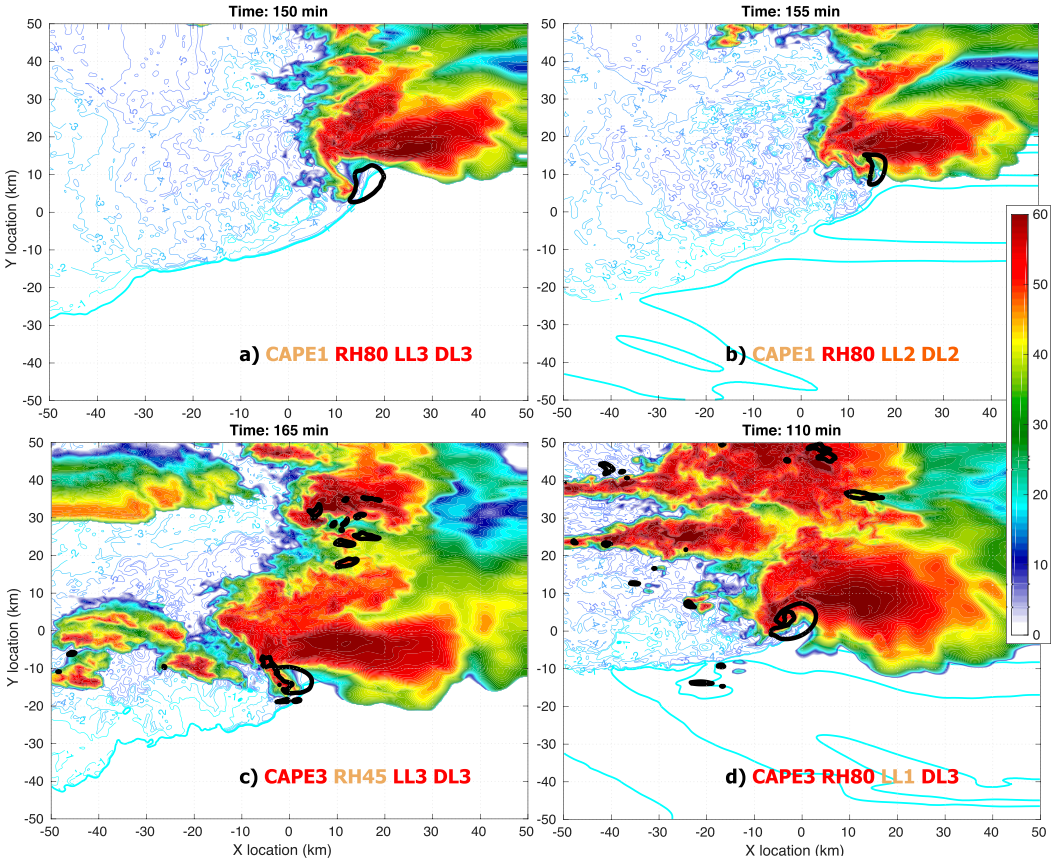

FIG. 2. Simulated radar reflectivity factor at 1 km AGL (shading; dBZ), surface temperature difference from the initial model profile (blue contours at intervals of −1 K), and the 6 m s^{-1} 1–4-km mean vertical velocity contour (solid black line). (a) CAPE1_RH80_LL3_DL3 run at 150 min. (b) CAPE1_RH80_LL2_DL2 run at 155 min. (c) CAPE3_RH45_LL3_DL3 run at 165 min. (d) CAPE3_RH80_LL1_DL3 run at 110 min.

$$\frac{dw_{\mathrm{EBPA,only}}}{dt} = \frac{1}{2}\frac{d(w^2_{\mathrm{EBPA,only}})}{dz} = B - \frac{1}{\rho_0}\frac{\partial p'_b}{\partial z}, \tag{5}$$

$$\frac{dw_{B,\mathrm{only}}}{dt} = \frac{1}{2}\frac{d(w^2_{B,\mathrm{only}})}{dz} = B. \tag{6}$$

These equations were vertically integrated along trajectory paths to obtain $w_{\mathrm{EBPA,only}}$ and $w_{B,\mathrm{only}}$. Note that $w_{\mathrm{EBPA,only}} \neq w_{\mathrm{EBPA}}$ and $w_{B,\mathrm{only}} \neq w_B$. For instance, because w_B depends on the time integral of buoyant forcing along a trajectory path, this quantity depends on the time it takes a parcel to travel between two points. Since that time is determined by all the accelerations acting upon the air parcel (not just buoyancy), w_B is implicitly influenced by the other pressure forcing terms. In contrast, $w_{B,\mathrm{only}}$ does not depend on other forcing terms. The quantities $r_{\mathrm{EBPA}} \equiv 100\{[\max(w_{\mathrm{NET}}) - \max(w_{\mathrm{EBPA,only}})]/\max(w_{\mathrm{EBPA,only}})\}$ and $r_B \equiv 100\{[\max(w_{\mathrm{NET}}) - \max(w_{B,\mathrm{only}})]/\max(w_{B,\mathrm{only}})\}$ facilitate the assessment of the contributions of different accelerations to $w_{\max}$. For instance, $r_{\mathrm{EBPA}} = 50\%$ indicates that DPA increases the maximum vertical velocity to a value that is 50% larger than it would have been if EBPA were acting alone. Likewise, $r_B = -50\%$ indicates that DPA and BPA reduces the maximum vertical velocity to a value that is 50% smaller than it would have been if B were acting alone.

3. Results from numerical simulations

a. *Overview of simulations*

Most of the simulations produced prolonged isolated right-moving storms with supercell structures apparent in simulated radar reflectivity fields (e.g., Figs. 2a–d), including hook echoes and bounded weak-echo regions. There were several exceptions; in the runs with the lowest CAPE and RH, initial updrafts did not persist beyond 1–1.5 h. In the runs with the highest CAPE, lowest deep-layer shear, and low to moderate magnitudes of low-level shear, supercells were generally overrun by their outflow during the last hour of the

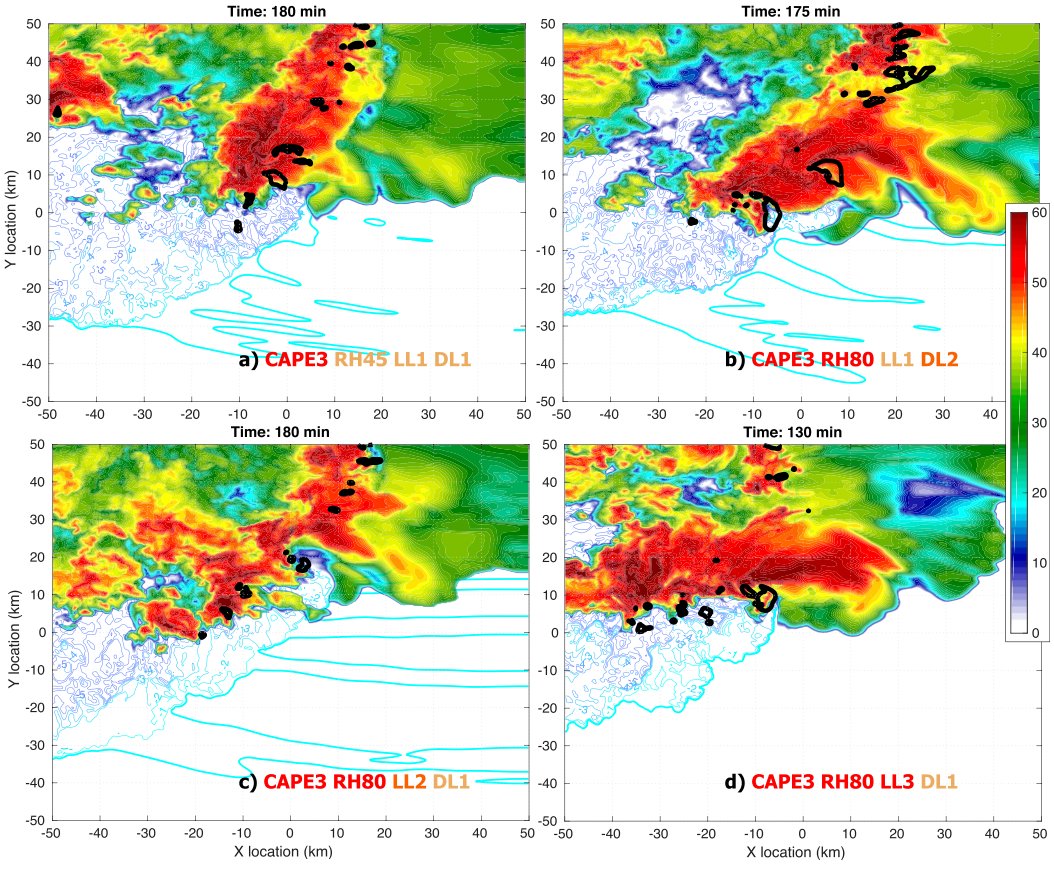

FIG. 3. As in Fig. 2, but for (a) CAPE3_RH45_LL1_DL1 run at 180 min, (b) CAPE3_RH80_LL1_DL2 run at 175 min, (c) CAPE3_RH80_LL2_DL1 run at 180 min, and (d) CAPE3_RH80_LL3_DL1 run at 130 min.

simulations and became disorganized multicellular clusters (e.g., Figs. 3a–c). This complicated the updraft tracking during the last hour of these simulations such that parts of them were omitted from further analysis. Furthermore, in the runs with the highest CAPE, highest low-level shear, and weakest deep-layer shear, a tight grouping of multiple supercell storms formed around the initial right mover during the last hour. This also made updraft tracking difficult, and parts of these runs were consequently omitted from further analysis (e.g., Fig. 3d). Finally, a visual inspection of the output fields from all simulations affirmed that any lateral boundary related distortions remained substantially removed from the primary supercell updraft. In contrast with the supercell runs, the LOWSHR runs produced a region of disorganized multicellular convection and a radially spreading cold pool (not shown). Statistics from the LOWSHR runs are omitted from some subsequent plots because updraft tracking, and the subsequent assessment of updraft width, inflow, and SR flow, was not possible given the disorganized nature of the LOWSHR convection. However, characteristics of buoyancy, w and trajectory analyses from the LOWSHR runs are compared to the supercell runs.

b. *Bulk comparisons of quantities among runs*

In subsequent discussion, linear Pearson correlation coefficients C are referred to as "strong" if $|C| > 0.7$ and "moderate" if $0.5 \leq |C| < 0.7$. Quantities were averaged over the lifetime of supercells and then correlated among runs. All C values were statistically significant to the 99% confidence level based on the Student's t test. To assess the relationship between SR flow and inflow, two 0–3-km average SR flow estimates were used in conjunction with the motion of tracked updrafts. The first SR flow used the wind in the initial model profile (SR_I), and was strongly correlated ($C = 0.87$) with inflow in the 0–4-km layer (Fig. 4a). The second SR flow estimate used the average of the horizontal wind in a 7.5 km × 7.5 km box with the northwest corner of the box located at the updraft center point (SR_E), and was even more strongly correlated ($C = 0.94$) with inflow in the 0–4-km layer (Fig. 4b). Inflow in

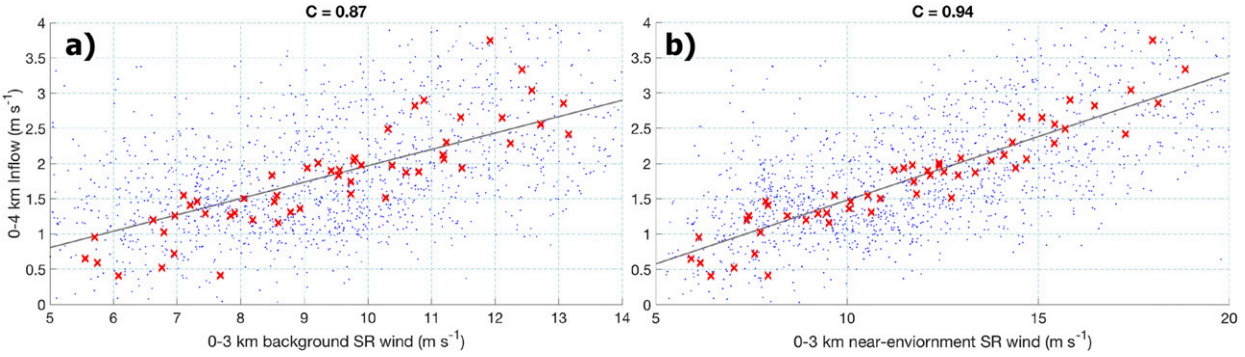

FIG. 4. Scatterplots of instantaneous quantities from 5-min model output (blue dots) and quantities averaged over simulations (red markers). (a) 0–3-km SR_I (x axis; m s^{-1}) and 0–4-km inflow (y axis; m s^{-1}). (b) As in (a), but for the 0–3-km SR_E (x axis; m s^{-1}). Correlation coefficients C rounded to two decimal points are listed above the panels.

the 0–4-km layer was used in lieu of the 0–3-km layer because air parcels typically underwent gradual ascent as they approached the updraft (i.e., parcels starting at 3 km entered the updraft at closer to 4 km). Because low-level SR flow is determined by the storm motion relative to the low-level hodograph, these strong correlations indicate that storms moving away from their low-level hodographs at faster rates had larger inflow than storms moving away from their low-level hodographs at slower rates.

Inflow in the 0–4-km layer was strongly correlated with 1–10-km average effective updraft radius R_{eff} ($C = 0.9$; Fig. 5a), affirming that updrafts with larger SR flow and inflow were wider than those with smaller SR flow and inflow. Averages over the 5–12-km layer of level-maximum tracer concentrations were strongly correlated with updraft width ($C = 0.9$; Fig. 5b), indicating that wider updrafts were able to transport higher concentrations of boundary layer air into the middle to upper troposphere than narrower updrafts.

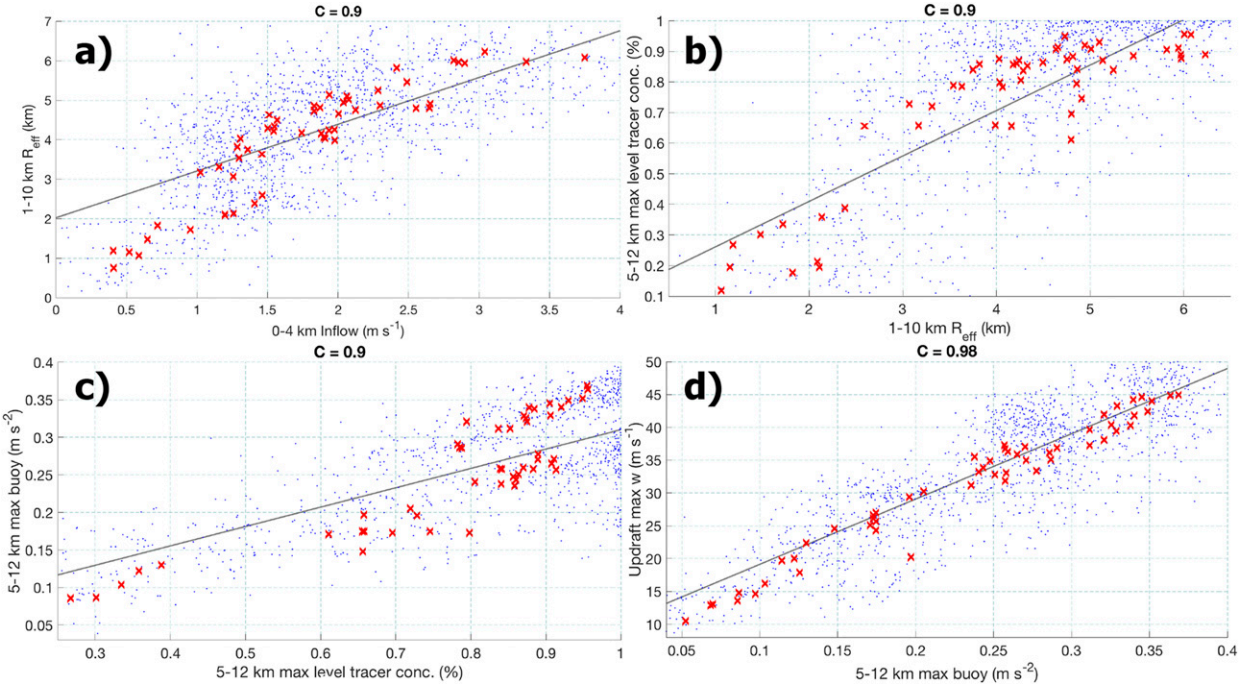

FIG. 5. As in Fig. 4, but for (a) the 0–4-km inflow (x axis; m s^{-1}) and the 1–10-km effective updraft radius R_{eff} (y axis; km), (b) the 1–10-km R_{eff} (x axis; km) and the 5–12-km mean of the layer maximum tracer concentration (y axis; %), (c) the 5–12-km mean of the layer maximum tracer concentration (x axis; %) and the 5–12-km mean of the layer maximum buoyancy (y axis; m s^{-2}), and (d) the 5–12-km mean of the layer maximum buoyancy (x axis; m s^{-2}) and the maximum updraft vertical velocity (y axis; m s^{-2}).

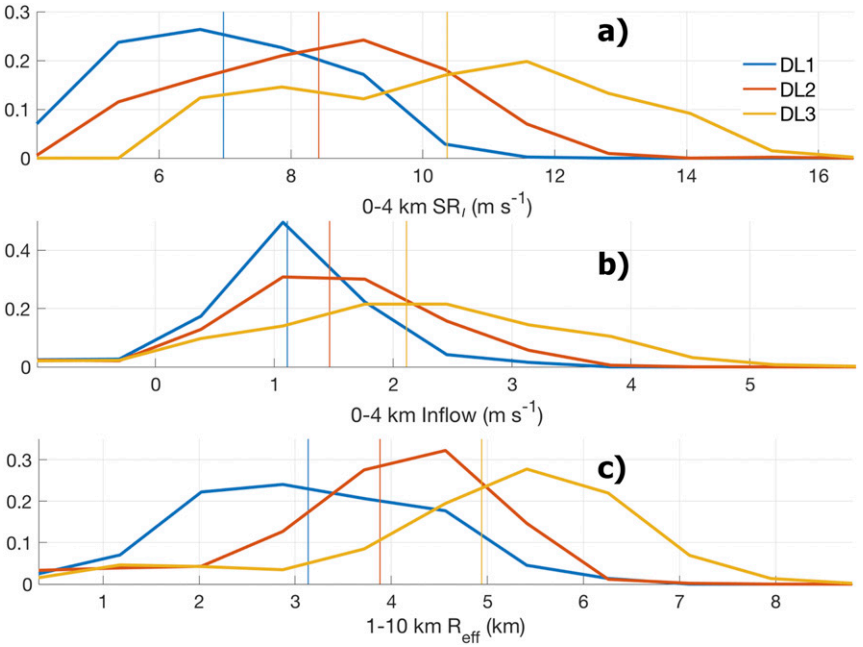

FIG. 6. Histograms of model fields in 5-min output from the DL1 runs (solid blue lines), the DL2 runs (solid red lines), and the DL3 runs (solid yellow lines), with averages of the DL1, DL2, and DL3 runs shown as thin vertical lines. (a) 0–3-km SR_l ($m\,s^{-1}$). (b) 0–4-km inflow ($m\,s^{-1}$). (c) 1–10-km R_{eff} (km). A given histogram curve is normalized by the sum of all 5-min output times represented by that curve.

The magnitudes of 5–12-km-layer level-maximum tracer concentrations were strongly correlated with 5–12-km-layer level-maximum buoyancy ($C = 0.9$; Fig. 5c), indicating that updrafts with the highest concentrations of boundary layer air also had the largest buoyancy maxima. Finally, 5–12-km-layer level-maximum buoyancy was well correlated with updraft maximum vertical velocities, indicating that the most buoyant updrafts were also the strongest ($C = 0.98$; Fig. 5d).

Storms in environments with stronger deep-layer shear had larger low-level SR flow (Fig. 6a) and inflow (Fig. 6b) than storms in weaker deep-layer shear. This occurred because the stronger steering current associated with the deep-layer shear causes a greater deviation between the storm motion and the low-level hodograph than storms experiencing weaker deep-layer shear. Storms in environments with stronger deep-layer shear were relatedly wider than storms in environments with weaker deep-layer shear (Fig. 6c). For given values of CAPE, supercell simulations with progressively larger deep-layer shear had progressively larger buoyancy (Figs. 7a–c) and w (Figs. 8a–c), and Figs. 4 and 5 show that these differences in buoyancy were correlated with differences in SR flow, inflow, and updraft width shown in Figs. 6a–c.

To compare the LOWSHR runs (wherein updrafts were not tracked) to the supercell simulations in the analysis described next, we found the horizontal location of the domain maximum w at each time and then found the maximum buoyancy and w within a 2-km-wide box centered at the location of maximum w, and then averaged from 5 to 12 km to produce the analogous quantities that were computed within the tracked updrafts (hereafter $B_{5–12km}$ and $w_{5–12km}$). For given values of CAPE, $B_{5–12km}$ (Figs. 7a–c) and $w_{5–12km}$ (Figs. 8a–c) in the LOWSHR runs were considerably smaller than in the supercell runs.

From this analysis of 5–12-km averages, we cannot rule out contributions to these w differences from DPA in line with the dynamic hypothesis. However, strong correlations between updraft inflow, width, buoyancy, and maximum w shown in Fig. 5 are consistent with the thermodynamic hypothesis. In fact, differences in 5–12-km average buoyancy and w between the LOWSHR and strongly sheared supercell runs for given values of CAPE are of similar magnitude to differences in updraft buoyancy and w in runs with large differences in CAPE (Figs. 7d and 8d). This supports the idea that shear, storm inflow, and updraft width strongly modulate updraft buoyancy.

c. *Trajectory analysis*

We obtained a total of 686 ''accurate'' trajectories that passed through the grid point of maximum vertical velocity w_{max} within updrafts among the supercell

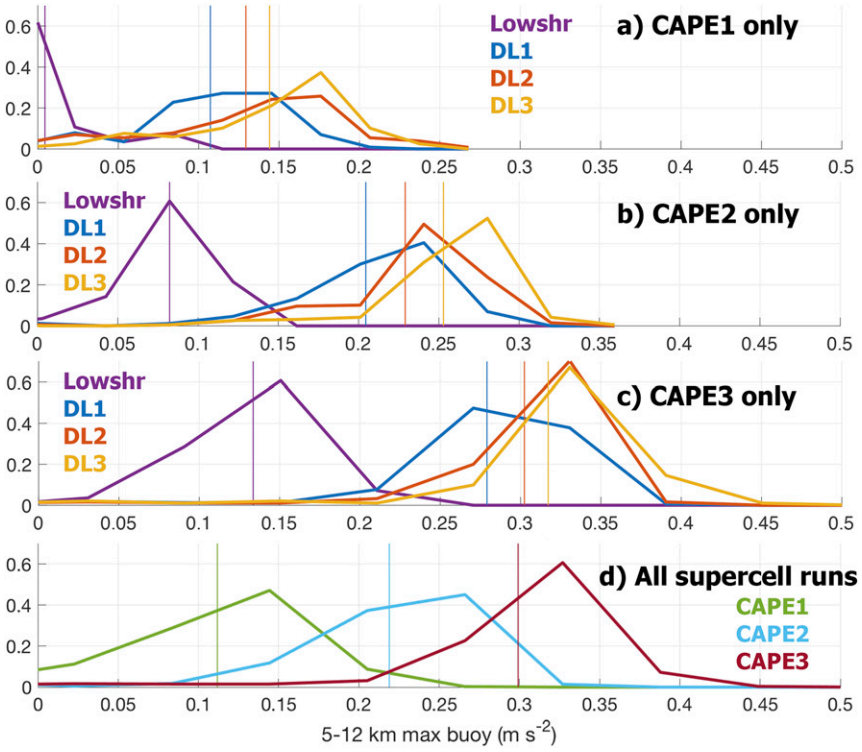

FIG. 7. (a)–(c) As in Fig. 6, but for the 5–12-km mean of the layer maximum buoyancy ($m\,s^{-2}$), with the LOWSHR runs included (purple). (a) CAPE1 runs only. (b) CAPE2 runs only. (c) CAPE3 runs only. (d) As in (a)–(c), but for the CAPE1 (green), CAPE2 (cyan), and CAPE3 (dark red) subsets of all runs.

simulations, and 156 from the LOWSHR simulations. These trajectories most frequently originated from the upper part of the boundary layer (Fig. 9a) where the most unstable CAPE was present in each initial sounding,[1] though they occasionally originated from entrained environmental air at higher altitudes. Altitudes of w_{max} ranged from 8 to 15 km (Fig. 9a), and w_{max} altitudes generally increasing with increasing CAPE. The overwhelming majority of trajectories originated from the southeast, and to a lesser extent the southwest, of the location of the maximum vertical velocity, which is the presumed ''inflow region'' of the updrafts (Fig. 9b).

In a manner loosely consistent with previous studies, $\max(w_{NET})$ was larger on average than $w_{EBPA,only}$ indicating dynamic enhancement of w_{max}, though the median percentages (as indicated by r_{EBPA}) of this enhancement for selected subsets of simulations were near or less than 10% aside from the DL3 runs (Fig. 10a) and the CAPE1 runs (Fig. 10c). Among the subgroups of supercell runs, medians of $r_{EBPA,DL3} > r_{EBPA,DL2} > r_{EBPA,DL1}$ (≈10%, 5%, and 0%, respectively; Fig. 10a) indicating that progressively larger shear magnitudes led to progressively larger DPA enhancement r_{EBPA}. Additionally, medians of $r_{EBPA,CAPE1} > r_{EBPA,CAPE2} > r_{EBPA,CAPE3}$ (≈30%, 10%, and 7.5%, respectively; Fig. 10c) indicating that less buoyant updrafts were more dynamically enhanced than more buoyant updrafts.

The interpretation becomes more complicated, however, when we compare $\max(w_{NET})$ and $\max(w_{B,only})$ (Figs. 10b,d). Although along some trajectories $\max(w_{NET}) > \max(w_{B,only})$, more frequently $\max(w_{NET}) < \max(w_{B,only})$ leading to medians of r_B between 0% and −10% for all subgroups of runs. Furthermore, even for the trajectories where $\max(w_{NET}) > \max(w_{B,only})$ (i.e., the dots to the left of the $r_B = 0$ line), which indicates that their vertical velocities were substantially enhanced by pressure accelerations, $\max(w_{NET})$ was conspicuously constrained by $\sqrt{2CAPE}$ for a given environment (indicated by most points with a given color in Figs. 10c and 10d residing near or below the position of the horizontal line of that color). There were only a few rare instances of parcels exceeding their thermodynamic speed limit in the CAPE2 runs, and these instances made up a very small percentage

[1] Note that the presence of MUCAPE at the top of the boundary layer is a somewhat unique characteristic of the WK82 sounding, and is not necessarily representative of all supercell environments.

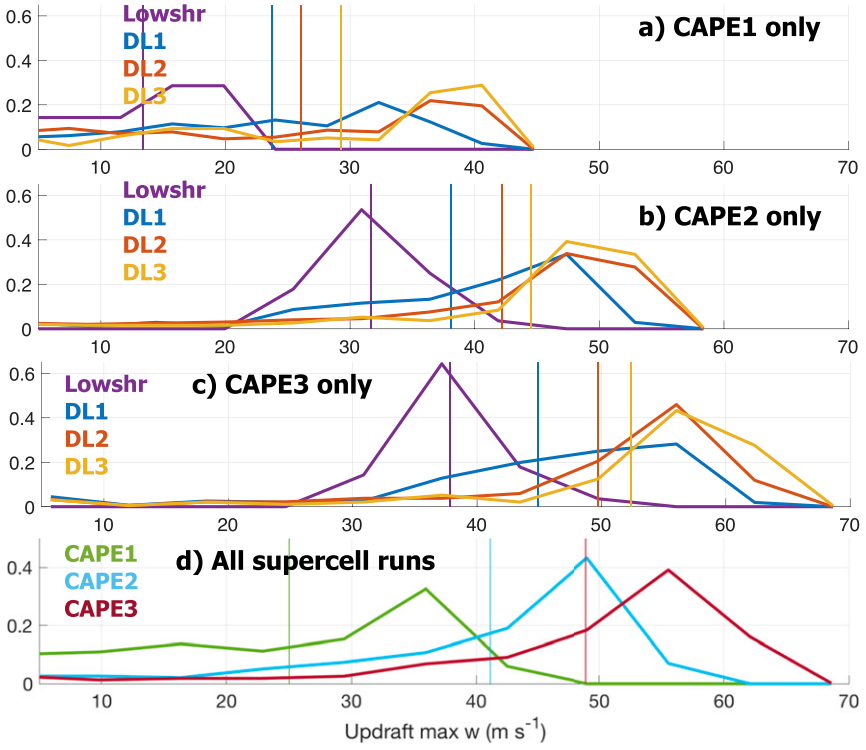

FIG. 8. As in Fig. 7, but for the 5–12-km mean of the layer maximum w.

of the trajectories studied. This suggests that the net acceleration along an air parcel's path was capped by (and largely determined by) the updraft's core buoyancy, whereas the individual percentages of DPA, BPA, and B that contributed to this net acceleration were determined by what regions within the updraft that the air parcel happened to pass through. The idea that w_{NET} is regulated by the updraft's maximum buoyancy is supported by the strong correlation between these two quantities in Fig. 5d.

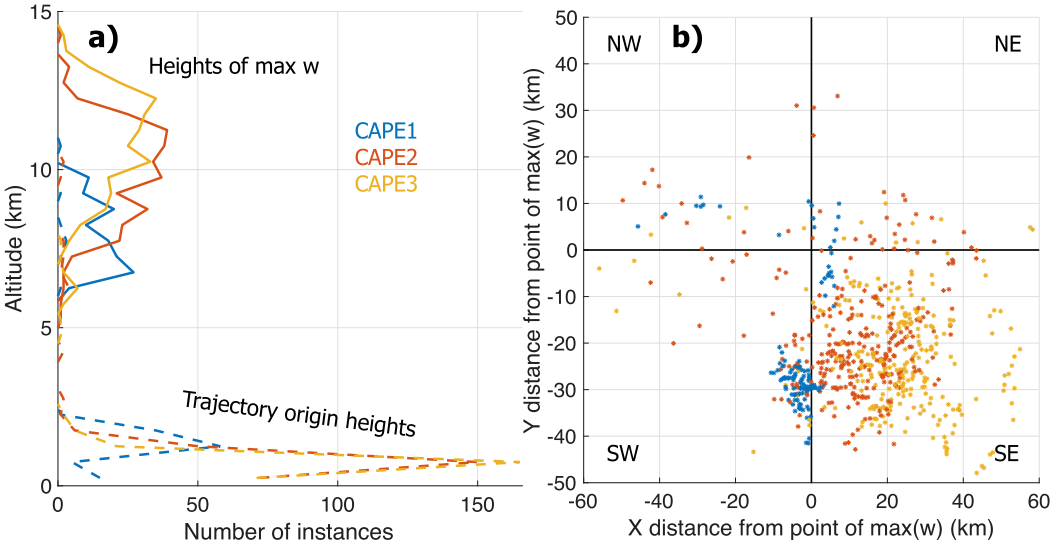

FIG. 9. (a) Histograms of the number of locations of the maximum w_{NET} along trajectories (solid lines) and the number of trajectory origin points (dashed lines) that fall within 500-m-wide height bins. (b) Scatterplot of the origin locations of trajectories. CAPE1 runs (blue), CAPE2 runs (red), and CAPE3 runs (yellow).

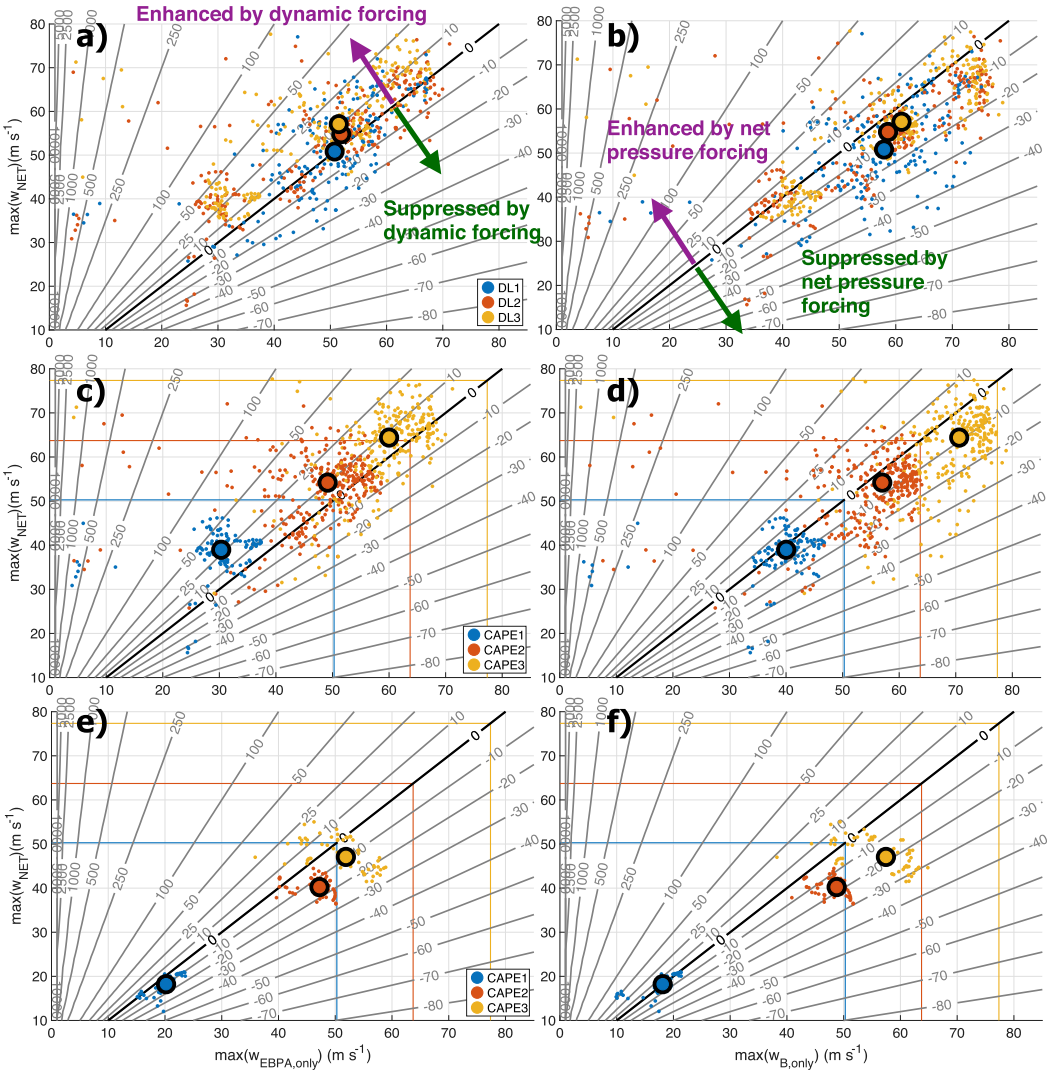

FIG. 10. (left) Scatterplots (small dots) of max($w_{\mathrm{EBPA,only}}$) (x axis; m s^{-1}) vs max(w_{NET}) (y axis; m s^{-1}) from all "accurate" trajectories. (right) As in the left panels, but with max($w_{B,\mathrm{only}}$) on the x axis. Gray contours are r_{EBPA} in the left panels and r_B in the right panels. Medians for a given set of simulations are large dots with black edges. (a),(b) DL1 (blue), DL2 (red), and DL3 (yellow) runs. (c),(d) CAPE1 (blue), CAPE2 (red), and CAPE3 (yellow) runs. (e),(f) LOWSHR CAPE1 (blue), CAPE2 (red), and CAPE3 (yellow) runs. The $\sqrt{2\mathrm{MUCAPE}}$ (where MUCAPE is most unstable CAPE) is shown as solid blue, red, and yellow lines for CAPE1, CAPE2, and CAPE3, respectively.

It is possible that in ordinary nonrotating updrafts, the absence of rotationally driven upward DPA results in net pressure forcing substantially reducing max(w) from the magnitude it would have if buoyancy were acting alone (i.e., $r_B \ll 0$). This would further suggest that the advantage of supercellular updrafts over nonsupercellular updrafts is the DPA enhancement to max(w), which may compensate for downward oriented BPA. To address this idea, analogous trajectories were also run through the domain maximum w in the LOWSHR runs (Figs. 10e,f). Values of r_{EBPA} along these trajectories were closer to −10% indicating that parcels were modestly dynamically suppressed in the LOWSHR runs, and r_B values were closer to −15%. This means that pressure gradient forces generally weakly suppressed the LOWSHR updrafts. The comparison between the r_{EBPA} and r_B values in the supercell runs and the LOWSHR runs provides support for the dynamic hypothesis, in that while nonsupercellular updrafts were suppressed by dynamic forcing, supercell updrafts were weakly enhanced by dynamic forcing. Furthermore, while total pressure accelerations suppressed buoyant accelerations in both supercells and nonsupercells, r_B was slightly smaller in

the nonsupercell updrafts indicating that this suppressive effect was slightly stronger for nonsupercellular convection. However, the core buoyancy for a given CAPE value was notably smaller in the LOWSHR runs than in the supercell runs, so that max($w_{B,\text{only}}$) for each CAPE value was roughly 10 m s^{-1} slower. This further indicates that while there was some dynamic enhancement in the supercells, there were also very large differences in buoyant forcing between the supercells and nonsupercells. These large differences in buoyant accelerations led to comparable or larger differences in $w_{\max}$ between the supercells and nonsupercells than the differences in $w_{\max}$ imparted by the differences in DPA between the supercells and nonsupercells.

Composites of the vertical profiles of terms from Eq. (2) show generally larger upward DPA through the updraft in supercells (Fig. 11a) than in the nonsupercells (Fig. 11b), but also much larger downward BPA in the supercell simulations along with much larger upward buoyancy accelerations in the supercell runs. Consequently, the greater buoyancy and dynamic forcing of parcels in the supercell updrafts was somewhat offset by larger downward BPA, consistent with the very small differences in r_B between the supercell and nonsupercell updrafts (Figs. 10d,f). The large offsetting contributions to max(w_{NET}) by DPA and BPA are noteworthy, and likely result from the fact that both p_b (e.g., Morrison 2016a) and p_d (e.g., Davies-Jones 2002) scale positively with the updraft width and updraft buoyancy. The connection between p_d and updraft buoyancy results from the dependence of p_d on the updraft's wind field, and the dependence of the updraft's wind field on accelerations from B and p_d [see the discussion related to Eq. (3.3.d) in Davies-Jones (2002)]. Therefore, consistent with the strong correlations between updraft buoyancy and w in Fig. 5d and the degree to which max(w_{NET}) is constrained by the max($w_{B,\text{only}}$) in Fig. 10, larger buoyancy and width of supercells than nonsupercells at least partially contributed to larger DPA in supercells.

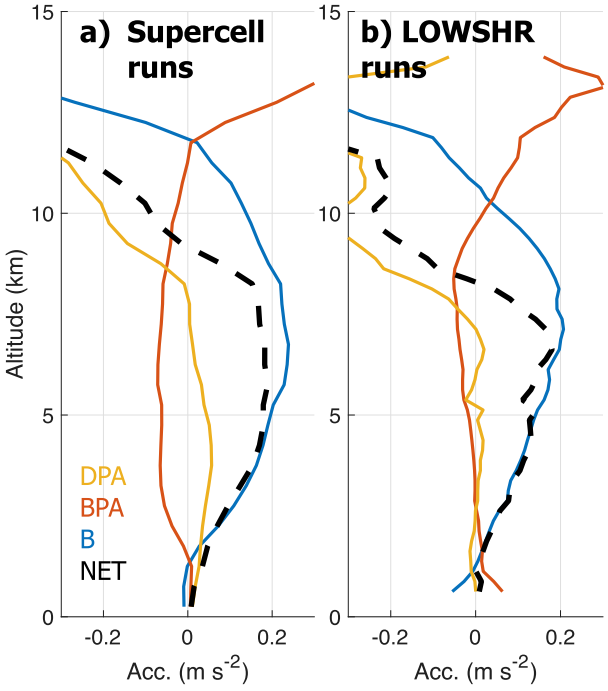

FIG. 11. Composite vertical profiles along trajectories of B (m s^{-2}; blue lines), BPA (m s^{-2}; red lines), DPA (m s^{-2}; yellow lines), and the sum of all vertical acceleration terms (black dashed lines) from (a) the supercell runs and (b) the LOWSHR runs.

4. Theoretical interpretation of the relationship between inflow and updraft width

The previous section demonstrated a close connection between horizontal inflow speed and updraft width, and in turn strong correlation between updraft width, buoyancy, and vertical velocity. In this section we explain the dynamics responsible for the positive correlations between inflow and updraft width using simple expressions derived from the Boussinesq governing momentum and mass continuity equations. While the anelastic approximation provides a more accurate equation set to describe the dynamics of deep convection, previous authors have shown that accurate representations of vertical velocity in deep convection are obtainable from the Boussinesq equations (e.g., Morrison 2016a,b; Peters 2016). The Boussinesq w and continuity equations in cylindrical coordinates relative to the updraft center are

$$0 = -\frac{1}{r}\frac{\partial(ruw)}{\partial r} - \frac{1}{r}\frac{\partial(wv)}{\partial \phi} - \frac{\partial(w^2)}{\partial z} - \alpha_0\frac{\partial p'}{\partial z} + B, \quad (7)$$

$$0 = \frac{1}{r}\frac{\partial(ru)}{\partial r} + \frac{1}{r}\frac{\partial v}{\partial \phi} + \frac{\partial w}{\partial z}, \quad (8)$$

where u is the radial wind, r is the radial distance from the center of the updraft, v is the tangential wind, ϕ is an azimuthal angle, α_0 is a constant specific volume, w is the vertical wind, z is the vertical coordinate, and B is buoyancy.

Horizontally averaging Eqs. (7) and (8) over the updraft, defining the horizontal average of an arbitrary variable ϑ at a given height as $\overline{\vartheta} \equiv [1/(\pi R^2)]\int_{r=0}^{r=R}\int_{\phi=0}^{\phi=2\pi} r\vartheta\, d\phi\, dr$, $\vartheta'' = \vartheta - \overline{\vartheta}$, and R as a radius where the azimuthal average of w vanishes, gives

$$0 = -\frac{\partial \overline{w^2}}{\partial z} - \alpha_0 \frac{\partial \overline{p'}}{\partial z} + \overline{B} - \frac{\partial (\overline{w''^2})}{\partial z} - R\tilde{u}\tilde{w} - R\widetilde{u''w''}, \quad (9)$$

$$0 = \frac{2}{R}\tilde{u}|_{r=R} + \frac{\partial \overline{w}}{\partial z}, \quad (10)$$

where $\tilde{u}|_{r=R}$ is the azimuthal average of u evaluated at $r = R$. Note that we may neglect $R\tilde{u}\tilde{w}$ because $\tilde{w}$ vanishes at $r = R$. We will also neglect $R\widetilde{u''w''}$ because previous authors have shown that turbulent horizontal mixing of vertical momentum has a negligible effect on the cloud-averaged vertical momentum budget (De Roode et al. 2012; Sherwood et al. 2013; Morrison 2017).

Next, we take $\int_{z=z_0}^{z=z_0+H}(\cdot)\,dz$ of Eqs. (9) and (10), where z_0 is the height near the updraft "base" where w vanishes, and $z_0 + H$ is an arbitrary height within the updraft. Evaluating these integrals and defining the vertical average of ϑ as $\hat{\vartheta} \equiv (1/H)\int_{z=z_0}^{z=z_0+H}\vartheta\,dz$ and $\Delta\overline{p'} \equiv \overline{p'}|_{z=z_0+H} - \overline{p'}|_{z=z_0}$ gives

$$0 = \overline{w^2}|_{z=z_0+H} + \alpha_0 \Delta\overline{p'} - \widehat{\overline{B}}H + \overline{w''^2}|_{z=z_0+H}, \quad (11)$$

$$0 = \frac{2H}{R}\widehat{\tilde{u}}|_{r=R} + \overline{w}|_{z=z_0+H}. \quad (12)$$

Here we assume that R is constant between heights z_0 and $z_0 + H$, which is supported by the simulations. It is also assumed that $\overline{w^2}|_{z=z_0+H} = \beta_1 \overline{w}^2|_{z=z_0+H}$, where β_1 is an empirically obtained constant of order 1. Henceforth, $\overline{w}^2$ is that at $z = z_0 + H$, and $\widehat{\overline{u}}_r$ is that at $r = R$. We additionally assume that $\overline{w^2}$ and $\overline{w''^2}$ vanish at $z = z_0$. Similar to Morrison (2017), $\overline{w''^2}|_{z=z_0+H}$ is approximated by applying a simple first-order eddy diffusion approach giving $\overline{w''^2}|_{z=z_0+H} \approx -k^2L^2(\partial\overline{w}/\partial z)^2 \approx -k^2L^2(\overline{w}^2/H^2)$, where the vertical derivative of $\overline{w}$ is approximated by linear gradients of $\overline{w}$ between z_0 and $z_0 + H$. Here $k^2 \approx 0.07$ is a mixing coefficient and $L \sim R$ is an eddy mixing length. As discussed below, we are concerned with H of several kilometers, meaning that the vertical mixing term is of order $0.1\overline{w}^2$. This term is therefore $\ll \beta_1\overline{w}^2$ and hereafter neglected. Using the aforementioned assumptions, combining Eqs. (11) and (12), and rearranging, we obtain

$$\overline{w}^2 = \beta_1^{-1}\left(\widehat{\overline{B}}H - \alpha_0\Delta\overline{p'}\right). \quad (13)$$

Equation (13) tells us that, perhaps unsurprisingly, w is largely determined by buoyancy and pressure gradient forces. The distribution of $\overline{B}$ within updrafts is straight forward to interpret (i.e., mostly positive), whereas the distribution of $\Delta\overline{p'}$ is comparatively complex and requires further examination. In the simulations there was typically nearly neutral p_b (Figs. 12a,b) and p_d near the surface (Figs. 12c,d), locally low p_b and p_d in the low to middle updraft, and locally high p_b and weakly negative to neutral p_d in the upper updraft. These pressure distributions resulted in locally low net perturbation pressure around 2–6-km height, locally neutral net pressure at the surface, and locally high net pressure in the upper updraft (Figs. 12e,f). The presence of locally neutral pressure in the lower updraft and locally high pressure in the upper updraft guaranteed that in every simulation, it was possible to find a height $z_0 + H$ where $\Delta\overline{p'} = 0$. The mean of this height was 8.8 km when averaged over the last 2 h of all runs, with a standard deviation of 1.6 km. Note that there were uncertainties in the assessment of the pressure at the bottom of the updraft needed to compute $\Delta\overline{p'} = 0$ because updrafts typically narrowed in the lowest few km and some of the lowest reaches of the updraft only contained a few grid points on a given level. The pressure at updraft base was therefore assumed to be the average in the lowest 500 m of the atmosphere horizontally averaged over the region where the 0–4-km mean w exceeded 3 m s^{-1}.

Physically, because $\Delta\overline{p'} = 0$ at height $z_0 + H$, any upward pressure acceleration up to this height in the lower updraft is directly compensated by an equal and opposite downward pressure acceleration. This is somewhat unsurprising given that net low pressure was centered near 4 km—below which upward pressure accelerations occurred and above which downward pressure acceleration occurred. At the height $z_0 + H$ where $\Delta\overline{p'} = 0$, Eq. (13) reduces to

$$\overline{w}^2 = \frac{\widehat{\overline{B}}H}{\beta_1}, \quad (14)$$

illustrating that at $z = z_0 + H$, $\overline{w}$ depends only on the updraft's buoyancy. Combining Eqs. (14) and (12) and solving for R gives

$$R = -2\widehat{\overline{u}}_r\left(\frac{\beta_1 H}{\widehat{\overline{B}}}\right)^{1/2}, \quad (15)$$

where $\widehat{\overline{u}}_r < 0$ for inflow, yielding positive R. It is apparent from Eq. (15) that for constant $\beta_1 H$, updraft width R is directly proportional to inflow and inversely proportional to buoyancy. Physically, it follows that given two updrafts with the same $\widehat{\overline{B}}$ and $\beta_1 H$ but different low-level inflow, the updraft with larger low-level inflow must be wider at H to maintain mass continuity. Likewise, an explanation for the inverse relationship between $\overline{B}$ and R is that given two updrafts with the same low-level inflow and $\beta_1 H$ but different buoyancies, the updraft with larger buoyancy must be narrower at H to maintain mass continuity.

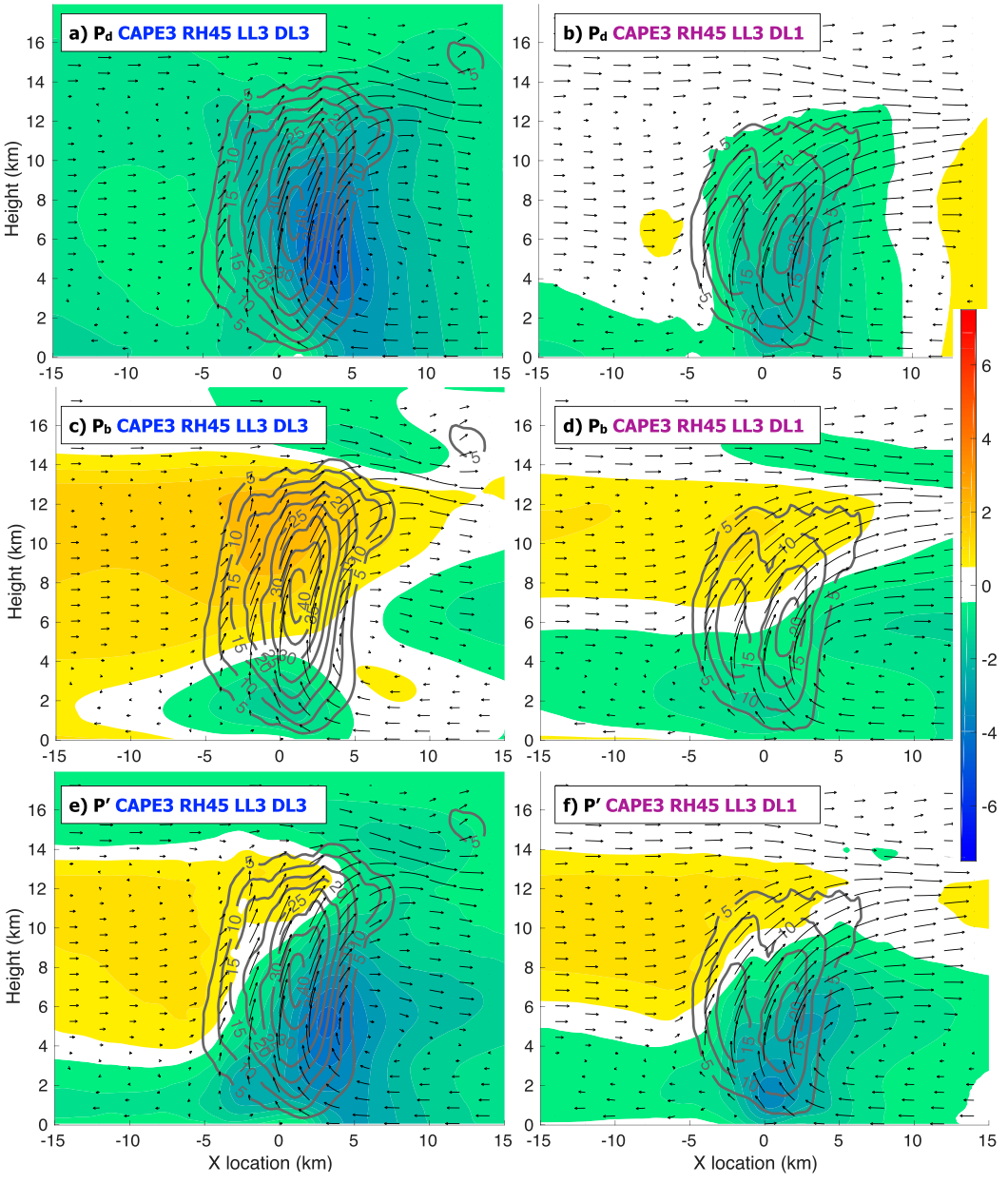

FIG. 12. Cross sections in the x and z directions averaged from 5 km south to 5 km north of updraft centers during the last 2 h of simulations of (a),(b) p_d (hPa), (c),(d) p_b (hPa), and (e),(f) p' (hPa), with streamlines (black arrows) and vertical velocity contours (gray; intervals of 5 m s^{-1}). (left) CAPE3_RH45_LL3_DL3 simulation and (right) CAPE3_RH45_LL3_DL1.

Central to both the derivation and interpretation of Eq. (15) is that R is approximately constant with height. Updraft widths from the simulations varied relatively little with height above the lowest 3 km of the atmosphere (e.g., Fig. 12). Thus, while conclusions obtained from Eqs. (14) and (15) may seem limited given that these equations are only strictly valid at height $z_0 + H$, approximately constant R with height means that the constraint on updraft width at height H well describes the behavior of R at nearly all heights. Furthermore, even though $H\beta_1$ values were not constant among all simulations, they were poorly correlated with inflow (Fig. 13a). Equation (15) therefore well describes the relationship between inflow and R, which is further detailed below. Nevertheless, there is a competing effect in that the widest updrafts will be able to maintain larger buoyancy through their depth than narrower updrafts, because of reduced entrainment and dilution

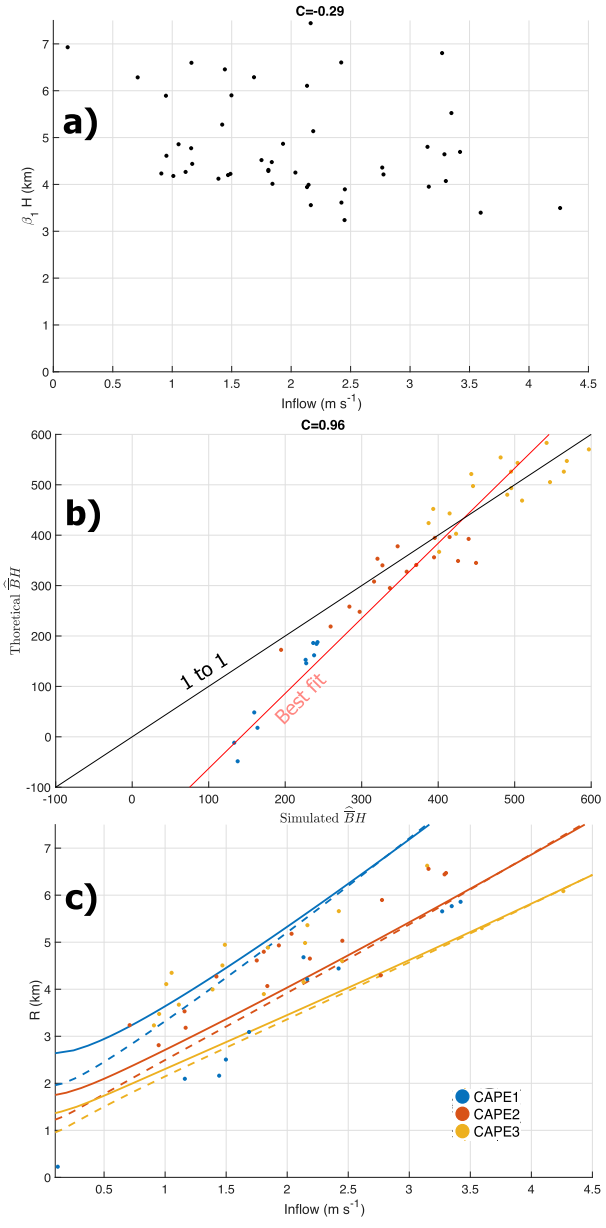

FIG. 13. (a) Inflow (x axis; m s^{-1}) vs $\beta_1 H$ from Eq. (15) (km). (b) Simulated vs theoretical [i.e., from Eq. (16)] $\widehat{BH}$ computed with $H = 8.8$ km, with the best-fit line shown in red and the 1-to-1 line shown in black. (c) Curves of the theoretical relationship between inflow and updraft radius [i.e., determined via Eq. (18)], with RH80 runs shown as dashed lines and RH45 runs shown as solid lines. Dots in all panels are averages for a simulation. Correlations C are shown above (a) and (b). In (b) and (c): CAPE1 is blue, CAPE2 is red, and CAPE3 is yellow.

(Morrison 2017; Hernandez-Deckers and Sherwood 2018). Thus, in the same thermodynamic environment strongly sheared wide storms are expected to be more buoyant than narrower storms experiencing weaker shear, which is indeed evident from the simulations as detailed in section 3. This relationship somewhat complicates the interpretation of the dependency of updraft radius on inflow, because *two updrafts of different widths are unlikely to have the same buoyancy*.

To account for effects of entrainment on B, we express $\widehat{\overline{B}}$ as a function of R following Morrison (2017). In that paper, an expression for buoyancy at the updraft center, B_c, was derived [Eq. (22) therein]:

$$B_c(z) = B_{\mathrm{AD}}(z) + \frac{\Omega_1}{R^2} + \frac{\Omega_2}{R^2} B_c(z), \tag{16}$$

where term $\Omega_2 \equiv -(k^2 Lz/\mathrm{P_r})$ represents the effect of the direct mixing of neutral environmental buoyancy into the cloud core, term $\Omega_1 \equiv -[2H_v g k^2 L/(c_p \mathrm{P_r})] \int_{z^*=\mathrm{LFC}}^{z^*=z} [q_{s,E}(1-\mathrm{RH}_E)]/\{T_E[1+(H_v^2 q_{s,E}/c_p R_v T_E^2)]\}\, dz^*$ represents the reduction of condensation rate and potential evaporation resulting from the mixing of dry environmental air into the cloud core, B_{AD} is the buoyancy of an air parcel lifted pseudoadiabatically from the level of free convection, P_r is the Prandtl number, H_v is the latent heat of vaporization, g is gravity, c_p is the specific heat of dry air at constant pressure, T_E is the temperature outside the updraft, RH_E is the relative humidity outside the updraft, and $q_{s,E}$ is the saturation mixing ratios outside of the updraft. As detailed in Morrison (2017), Eq. (16) quantifies the increase of buoyancy with R, and the decrease of buoyancy with decreasing RH_E. For $R \to 0$, $B_c(z) \le 0$ (assuming $\mathrm{RH}_E \le 1$). Likewise, as $R \to \infty$, $B_c(z) \to B_{\mathrm{AD}}(z)$.

To approximate $\widehat{\overline{B}}$, we assume that the horizontally averaged updraft buoyancy $\overline{B}$ is proportional to B_c at a given height such that $\widehat{\overline{B}} = \alpha B_c$, where α is a constant [similar assumptions were used in Morrison (2016a, 2017)]. We then vertically average Eq. (16) between z_0 and $z_0 + H$, assume that $\widehat{\Omega_2 B_c} \approx \widehat{\Omega}_2 \widehat{B_c}$, and solve for $\widehat{\overline{B}}$ giving

$$\widehat{\overline{B}} = \alpha \widehat{B_c(z)} = \frac{\alpha(R^2 \widehat{B_{\mathrm{AD}}} + \widehat{\Omega}_1)}{R^2 - \widehat{\Omega}_2}. \tag{17}$$

Values of the theoretical $\widehat{\overline{B}}$ from Eq. (17) using $\alpha = 1/3$, $L = 3000$ m, and the thermodynamic soundings from the simulations correspond reasonably well to the simulated $\widehat{\overline{B}}$, with a correlation coefficient of 0.96 (Fig. 13b). The theoretical $\widehat{\overline{B}}$ values are most similar to the simulations for CAPE2 and CAPE3, but are underpredicted for CAPE1.

Combining Eqs. (15) and (17) gives a quartic expression that relates R to the horizontal inflow $\widehat{u}_r$, H, β_1, α, L, and the parameters Ω_1 and Ω_2, which only depend on the environmental sounding. Solving for the only positive real root to this equation gives

$$R = \sqrt{\frac{-(\alpha\widehat{\Omega_1} - 4\widehat{\tilde{u}_r}^2\beta_1 H) + \sqrt{(\alpha\widehat{\Omega_1} - 4\widehat{\tilde{u}_r}^2\beta_1 H)^2 - 8\alpha\widehat{B_{AD}}\widehat{\tilde{u}_r}^2\beta_1 H\widehat{\Omega_2}}}{2\alpha\widehat{B_{AD}}}}. \quad (18)$$

Theoretical curves for R as a function of $\widehat{\tilde{u}_r}$ from Eq. (18) show a nearly linear relationship, and generally correspond well with the relationship between R and $\widehat{\tilde{u}_r}$ from the simulations (Fig. 13c), particularly for the CAPE2 sounding (here we take the updraft radius from the simulations to be R_{eff}). However, theoretical curves for the CAPE1 profile suggest that CAPE1 updrafts should be wider than CAPE2 and CAPE3 updrafts for a given inflow magnitude, whereas the simulated updrafts show, if anything, the opposite relationship. This discrepancy is consistent with the underprediction of the theoretical $\widehat{B}$ values for CAPE1 as seen in Fig. 13b, and does not alter the general interpretation of the relationship between inflow and updraft width.

5. Summary and discussion

Two hypotheses are evaluated in this paper for the relationship between deep-layer shear and the intensity of mid- to upper-level updrafts in supercells. The dynamic hypothesis states that supercells in strongly sheared environments have stronger dynamic pressure accelerations (largely due to updraft rotation) than those in less sheared environments and than ordinary convection in weakly sheared environments. Thus, stronger upward accelerations in supercells in a strongly sheared environment would be expected to enhance their maximum updraft speeds. The thermodynamic hypothesis states that the strong low-level, storm-relative flow in strongly sheared environments makes supercell updrafts wider than updrafts in environments with weaker shear. Because greater shear makes updrafts wider, it also makes them less susceptible to updraft-core dilution, which makes their buoyant accelerations stronger than updrafts in environments with weaker shear.

To test the validity of these hypotheses and their relevance in a variety of thermodynamic and kinematic environments, a large suite of horizontally homogeneous, idealized numerical simulations of supercell thunderstorms were performed and analyzed, wherein different combinations of environmental low-level shear, deep-layer shear, midlevel relative humidity, and low-level moisture/CAPE were explored. The conclusions drawn from the results of these simulations are summarized as follows:

- In supercells simulated over a variety of environments, low-level inflow into an updraft is well correlated with low-level storm-relative flow, inflow is well correlated with updraft width, updraft width is well correlated with updraft core buoyancy, and updraft buoyancy is well correlated with maximum updraft intensity. This supports the thermodynamic hypothesis.
- Theoretical arguments affirm that updraft width should increase with inflow, and that wider updrafts should have larger core buoyancy than narrower updrafts, because the cores of the former are less susceptible to entrainment-driven dilution.
- There is some evidence that dynamic accelerations in supercells enhance updraft speeds in supercells relative to nonsupercellular updrafts, supporting the dynamic hypothesis. This enhancement is only weakly dependent on the magnitude of deep-layer shear, and is most pronounced for updrafts in lower-CAPE environments. While dynamic accelerations increase with vertical wind shear, it is likely that at least part of this increase is itself due to wider, more buoyant, and stronger updrafts as well.
- Interestingly, the thermodynamic speed limit predicted by parcel theory is a fairly robust upper limit to the maximum updraft speed in supercells in all environments, despite the proportion of pressure accelerations and buoyant accelerations acting along air parcels' paths. Regardless of evidence that both the dynamic and thermodynamic hypotheses contribute to stronger updrafts in supercells, any increase in updraft speed due to enhanced dynamic accelerations is largely offset by stronger downward buoyancy pressure accelerations when buoyancy increases.

The results in this study clarify past uncertainty as to why the intensity of $w_{\max}$ in supercell updrafts stands out against other modes of convection. While the weakly sheared runs that were compared to supercells here by no means represent all the possible modes of nonsupercellular convection, there is compelling evidence from past literature that, unlike supercells, most other modes of convection are unable to loft nearly pure boundary layer air into the upper troposphere and are unable to achieve vertical velocities that are close to the thermodynamic speed limit. In large-eddy simulations of tropical convection, boundary layer air was strongly diluted well before it reached the tropopause (e.g., Romps and Kuang 2010). Furthermore, modeling studies of midlatitude mesoscale convective systems (MCSs) with similar model resolutions to those studied in this paper have not

shown boundary layer tracer concentrations that exceed 50%–75% in the upper troposphere (e.g., Parker 2008; French and Parker 2010; Lebo and Morrison 2015), and show maximum vertical velocities that only approach 75% of the thermodynamic speed limit. Maximum vertical velocities within the simulations studied here, on the other hand, were often 90%–100% of the thermodynamic speed limit (Figs. 10c,d). Of course, these studies did not comprehensively address the wide array of MCS morphologies, and further work is needed to fortify this comparison between supercells and MCSs.

In addition to the clear implications of maximum updraft speed on hail growth, lightning, and precipitation efficiency, these results have some application to supercell tornado forecasting. For instance, observational studies often show that stronger deep-layer shear, when combined with other favorable parameters, increases the likelihood of significant tornadoes, reflected in the fact that the significant tornado parameter incorporates measures of deep-layer shear (Thompson et al. 2007, 2012). Furthermore, Trapp et al. (2017) showed evidence that updraft width correlates with tornado width, so deep-layer shear may influence tornado size by virtue of the connection between shear and storm width discussed here. The fact that the updrafts simulated here in stronger shear are wider and stronger, and the dynamic pressure acceleration scales with updraft width and updraft velocity, means that wider updrafts in stronger deep-layer shear may have stronger low-level dynamic accelerations, irrespective of the low-level shear environment. These possibilities should be investigated in future work.

This work also has potentially broader reaching applications to cumulus parameterizations. A longstanding problem in cumulus parameterization has been the determination of factors that regulate cloud dimensions, including width. Cloud widths are important because they determine how much vertical mass flux a given cloud within a cloud ''ensemble'' contributes to the net vertical mass flux within a given global climate model or global weather forecast model grid cell (e.g., Arakawa and Schubert 1974). Furthermore, there has been a recent push toward the inclusion of organized convection in cumulus parameterizations (e.g., Moncrieff et al. 2017), which typically occurs in the presence of vertical wind shear. The demonstrated connection between environmental SR flow and vertical mass flux may be applicable to such parameterizations, since SR flow is dependent on the magnitude of vertical wind shear and a relationship can therefore be established between vertical wind shear and convective vertical mass flux. Finally, we have focused on the connection between *low-level* SR flow on storm dynamics here. Future work should investigate the effects of variations in upper-level SR flow on supercell updraft characteristics.

Acknowledgments. The authors are extremely grateful for excellent feedback from three anonymous peer reviewers. The CM1 source code was obtained online (http://www2.mmm.ucar.edu/people/bryan/cm1), and we are indebted to George Bryan for his tireless dedication to the development and distribution of this model. J. Peters's efforts were supported by the National Science Foundation (NSF) Grants AGS-1446342 and AGS-1928666, and C. Nowotarski's efforts were supported by NSF Grants AGS-1841674 and AGS-1928319. Additionally, J. Peters's efforts were partially supported by the Department of Energy Atmospheric Systems Research Grant DE-SC0000246356. The National Center for Atmospheric Research is sponsored by the National Science Foundation.

REFERENCES

Arakawa, A., and W. H. Schubert, 1974: Interaction of a cumulus cloud ensemble with the large-scale environment, part I. *J. Atmos. Sci.*, **31**, 674–701, https://doi.org/10.1175/1520-0469(1974)031<0674:IOACCE>2.0.CO;2.

Bryan, G. H., and J. M. Fritsch, 2002: A benchmark simulation for moist nonhydrostatic numerical models. *Mon. Wea. Rev.*, **130**, 2917–2928, https://doi.org/10.1175/1520-0493(2002)130<2917:ABSFMN>2.0.CO;2.

——, and H. Morrison, 2012: Sensitivity of a simulated squall line to horizontal resolution and parameterization of microphysics. *Mon. Wea. Rev.*, **140**, 202–225, https://doi.org/10.1175/MWR-D-11-00046.1.

Bunkers, M. J., B. A. Klimowski, R. L. Thompson, and M. L. Weisman, 2000: Predicting supercell motion using a new hodograph technique. *Wea. Forecasting*, **15**, 61–79, https://doi.org/10.1175/1520-0434(2000)015<0061:PSMUAN>2.0.CO;2.

Coffer, B. E., and M. D. Parker, 2015: Impacts of increasing low-level shear on supercells during the early evening transition. *Mon. Wea. Rev.*, **143**, 1945–1969, https://doi.org/10.1175/MWR-D-14-00328.1.

——, ——, J. M. L. Dahl, L. J. Wicker, and A. J. Clark, 2017: Volatility of tornadogenesis: An ensemble of simulated nontornadic and tornadic supercells in VORTEX2 environments. *Mon. Wea. Rev.*, **145**, 4605–4625, https://doi.org/10.1175/MWR-D-17-0152.1.

Davies-Jones, R., 2002: Linear and nonlinear propagation of supercell storms. *J. Atmos. Sci.*, **59**, 3178–3205, https://doi.org/10.1175/1520-0469(2003)059<3178:LANPOS>2.0.CO;2.

——, 2003: An expression for effective buoyancy in surroundings with horizontal density gradients. *J. Atmos. Sci.*, **60**, 2922–2925, https://doi.org/10.1175/1520-0469(2003)060<2922:AEFEBI>2.0.CO;2.

De Roode, S. R., A. P. Siebesma, H. J. Jonker, and Y. De Voog, 2012: Parameterization of the vertical velocity equation for shallow cumulus clouds. *Mon. Wea. Rev.*, **140**, 2424–2436, https://doi.org/10.1175/MWR-D-11-00277.1.

DiGangi, E. A., D. R. MacGorman, C. L. Ziegler, D. Betten, M. Biggerstaff, M. Bowlan, and C. K. Potvin, 2016: An overview of the 29 May 2012 Kingfisher supercell during DC3.

J. Geophys. Res. Atmos., **121**, 14 316–14 343, https://doi.org/10.1002/2016JD025690.

Doswell, C. A., III, and P. M. Markowski, 2004: Is buoyancy a relative quantity? *Mon. Wea. Rev.*, **132**, 853–863, https://doi.org/10.1175/1520-0493(2004)132<0853:IBARQ>2.0.CO;2.

Durran, D. R., and J. B. Klemp, 1983: A compressible model for the simulation of moist mountain waves. *Mon. Wea. Rev.*, **111**, 2341–2361, https://doi.org/10.1175/1520-0493(1983)111<2341:ACMFTS>2.0.CO;2.

French, A. J., and M. D. Parker, 2010: The response of simulated nocturnal convective systems to a developing low-level jet. *J. Atmos. Sci.*, **67**, 3384–3408, https://doi.org/10.1175/2010JAS3329.1.

Hannah, W. M., 2017: Entrainment versus dilution in tropical deep convection. *J. Atmos. Sci.*, **74**, 3725–3747, https://doi.org/10.1175/JAS-D-16-0169.1.

Hernandez-Deckers, D., and S. C. Sherwood, 2018: On the role of entrainment in the fate of cumulus thermals. *J. Atmos. Sci.*, **75**, 3911–3924, https://doi.org/10.1175/JAS-D-18-0077.1.

Holton, J. R., 1973: A one-dimensional cumulus model including pressure perturbations. *Mon. Wea. Rev.*, **101**, 201–205, https://doi.org/10.1175/1520-0493(1973)101<0201:AOCMIP>2.3.CO;2.

Jeevanjee, N., and D. M. Romps, 2016: Effective buoyancy at the surface and aloft. *Quart. J. Roy. Meteor. Soc.*, **142**, 811–820, https://doi.org/10.1002/qj.2683.

Kuo, H. L., and W. H. Raymond, 1980: A quasi-one dimensional cumulus cloud model and parameterization of cumulus heating and mixing effects. *Mon. Wea. Rev.*, **108**, 991–1009, https://doi.org/10.1175/1520-0493(1980)108<0991:AQODCC>2.0.CO;2.

Lebo, Z. J., and H. Morrison, 2015: Effects of horizontal and vertical grid spacing on mixing in simulated squall lines and implications for convective strength and structure. *Mon. Wea. Rev.*, **143**, 4355–4375, https://doi.org/10.1175/MWR-D-15-0154.1.

Lehmiller, G. S., H. B. Bluestein, P. J. Neiman, F. M. Ralph, and W. F. Feltz, 2001: Wind structure in a supercell thunderstorm as measured by a UHF wind profiler. *Mon. Wea. Rev.*, **129**, 1968–1986, https://doi.org/10.1175/1520-0493(2001)129<1968:WSIAST>2.0.CO;2.

Markowski, P. M., and Y. P. Richardson, 2014: The influence of environmental low-level shear and cold pools on tornadogenesis: Insights from idealized simulations. *J. Atmos. Sci.*, **71**, 243–275, https://doi.org/10.1175/JAS-D-13-0159.1.

——, C. Hannon, J. Frame, E. Lancaster, A. Pietrycha, R. Edwards, and R. L. Thompson, 2003: Characteristics of vertical wind profiles near supercells obtained from the Rapid Update Cycle. *Wea. Forecasting*, **18**, 1262–1272, https://doi.org/10.1175/1520-0434(2003)018<1262:COVWPN>2.0.CO;2.

McCaul, E. W., and M. L. Weisman, 1996: Simulations of shallow supercell storms in landfalling hurricane environments. *Mon. Wea. Rev.*, **124**, 408–429, https://doi.org/10.1175/1520-0493(1996)124<0408:SOSSSI>2.0.CO;2.

——, and C. Cohen, 2002: The impact of simulated storm structure and intensity of variations in the mixed layer and moist layer depths. *Mon. Wea. Rev.*, **130**, 1722–1748, https://doi.org/10.1175/1520-0493(2002)130<1722:TIOSSS>2.0.CO;2.

Moncrieff, M. W., C. Liu, and P. A. Bogenshultz, 2017: Simulation, modeling, and dynamical based parameterization of organized tropical convection for global climate models. *J. Atmos. Sci.*, **74**, 1363–1380, https://doi.org/10.1175/JAS-D-16-0166.1.

Morrison, H., 2016a: Impacts of updraft size and dimensionality on the perturbation pressure and vertical velocity in cumulus convection. Part I: Simple, generalized analytic solutions. *J. Atmos. Sci.*, **73**, 1441–1454, https://doi.org/10.1175/JAS-D-15-0040.1.

——, 2016b: Impacts of updraft size and dimensionality on the perturbation pressure and vertical velocity in cumulus convection. Part II: Comparison of theoretical and numerical solutions. *J. Atmos. Sci.*, **73**, 1455–1480, https://doi.org/10.1175/JAS-D-15-0041.1.

——, 2017: An analytic description of the structure and evolution of growing deep cumulus updrafts. *J. Atmos. Sci.*, **74**, 809–834, https://doi.org/10.1175/JAS-D-16-0234.1.

——, and J. M. Peters, 2018: Theoretical expressions for the ascent rate of moist convective thermals. *J. Atmos. Sci.*, **75**, 1699–1719, https://doi.org/10.1175/JAS-D-17-0295.1.

——, G. Thompson, and V. Tatarskii, 2009: Impact of cloud microphysics on the development of trailing stratiform precipitation in a simulated squall line: Comparison of one- and two-moment schemes. *Mon. Wea. Rev.*, **137**, 991–1007, https://doi.org/10.1175/2008MWR2556.1.

Mullendore, G. L., D. R. Durran, and J. R. Holton, 2005: Cross-tropopause tracer transport in midlatitude convection. *J. Geophys. Res.*, **110**, D06113, https://doi.org/10.1029/2004JD005059.

——, A. J. Homann, S. T. Jorgenson, T. J. Lang, and S. A. Tessendorf, 2013: Relationship between level of neutral buoyancy and dual-Doppler observed mass detrainment levels in deep convection. *Atmos. Chem. Phys.*, **13**, 181–190, https://doi.org/10.5194/acp-13-181-2013.

Parker, M. D., 2008: Response of simulated squall lines to low-level cooling. *J. Atmos. Sci.*, **65**, 1323–1341, https://doi.org/10.1175/2007JAS2507.1.

——, 2014: Composite VORTEX2 supercell environments from near-storm soundings. *Mon. Wea. Rev.*, **142**, 508–529, https://doi.org/10.1175/MWR-D-13-00167.1.

Peters, J. M., 2016: The impact of effective buoyancy and dynamic pressure forcing on vertical velocities within two-dimensional updrafts. *J. Atmos. Sci.*, **73**, 4531–4551, https://doi.org/10.1175/JAS-D-16-0016.1.

Potvin, C. K., and M. L. Flora, 2015: Sensitivity of idealized supercell simulations to horizontal grid spacing: Implications for Warn-on-Forecast. *Mon. Wea. Rev.*, **143**, 2998–3024, https://doi.org/10.1175/MWR-D-14-00416.1.

Romps, D. M., and Z. Kuang, 2010: Do undiluted convective plumes exist in the upper troposphere? *J. Atmos. Sci.*, **67**, 468–484, https://doi.org/10.1175/2009JAS3184.1.

Rotunno, R., and J. B. Klemp, 1982: The Influence of the shear-induced pressure gradient on thunderstorm motion. *Mon. Wea. Rev.*, **110**, 136–151, https://doi.org/10.1175/1520-0493(1982)110<0136:TIOTSI>2.0.CO;2.

Sherwood, S. C., D. Hernandez-Deckers, and M. Colin, 2013: Slippery thermals and the cumulus entrainment paradox. *J. Atmos. Sci.*, **70**, 2426–2442, https://doi.org/10.1175/JAS-D-12-0220.1.

Thompson, R. L., C. M. Mead, and R. Edwards, 2007: Effective storm-relative helicity and bulk shear in supercell thunderstorm environments. *Wea. Forecasting*, **22**, 102–115, https://doi.org/10.1175/WAF969.1.

——, B. T. Smith, J. S. Grams, A. R. Dean, and C. Broyles, 2012: Convective modes for significant severe thunderstorms in the contiguous United States. Part II: Supercell and QLCS tornado environments. *Wea. Forecasting*, **27**, 1136–1154, https://doi.org/10.1175/WAF-D-11-00116.1.

Trapp, R. J., G. R. Marion, and S. W. Nesbitt, 2017: The regulation of tornado intensity by updraft width. *J. Atmos. Sci.*, **74**, 4199–4211, https://doi.org/10.1175/JAS-D-16-0331.1.

Varble, A., and Coauthors, 2014: Evaluation of cloud-resolving and limited area model intercomparison simulations using TWP-ICE observations: 1. Deep convective updraft properties. *J. Geophys. Res. Atmos.*, **119**, 13 891–13 918, https://doi.org/10.1002/2013JD021371.

Wakimoto, R. M., H. Cai, and H. V. Murphey, 2004: The Superior, Nebraska, supercell during BAMEX. *Bull. Amer. Meteor. Soc.*, **85**, 1095–1106, https://doi.org/10.1175/BAMS-85-8-1095.

Warren, R. A., H. Richter, H. A. Ramsay, S. T. Siems, and M. J. Manton, 2017: Impact of variations in upper-level shear on simulated supercells. *Mon. Wea. Rev.*, **145**, 2659–2681, https://doi.org/10.1175/MWR-D-16-0412.1.

Weisman, M. L., and J. B. Klemp, 1982: The dependence of numerically simulated convective storms on vertical wind shear and buoyancy. *Mon. Wea. Rev.*, **110**, 504–520, https://doi.org/10.1175/1520-0493(1982)110<0504:TDONSC>2.0.CO;2.

——, and ——, 1984: The structure and classification of numerically simulated convective storms in directionally varying wind shears. *Mon. Wea. Rev.*, **112**, 2479–2498, https://doi.org/10.1175/1520-0493(1984)112<2479:TSACON>2.0.CO;2.

——, and R. Rotunno, 2000: The use of vertical wind shear versus helicity in interpreting supercell dynamics. *J. Atmos. Sci.*, **57**, 1452–1472, https://doi.org/10.1175/1520-0469(2000)057<1452:TUOVWS>2.0.CO;2.